Assessment of Carbon Sequestration in Forest Areas using Deep Learning

Raphael Duarte Britto

Dissertation presented to the School of Technology and Management of Bragança to obtain the Master Degree in Electrical and Computer Engineering. Work developed under the Dual Degree Program between the Polytechnic Institute of Bragança (IPB) and the Federal Center for Technological Education of Minas Gerais (CEFET-MG).

Work oriented by:

Prof. Doctor José Luís Sousa de Magalhães Lima

Prof. Doctor Ana Isabel Pinheiro Nunes Pereira

Prof. Doctor Eng. Murillo Ferreira dos Santos

Bragança

2025

Assessment of Carbon Sequestration in Forest Areas using Deep Learning

Raphael Duarte Britto

Dissertation presented to the School of Technology and Management of Bragança to obtain the Master Degree in Electrical and Computer Engineering. Work developed under the Dual Degree Program between the Polytechnic Institute of Bragança (IPB) and the Federal Center for Technological Education of Minas Gerais (CEFET-MG).

Work oriented by:

Prof. Doctor José Luís Sousa de Magalhães Lima

Prof. Doctor Ana Isabel Pinheiro Nunes Pereira

Prof. Doctor Eng. Murillo Ferreira dos Santos

Bragança

2025

Dedication

This work is dedicated to my parents and sister for their absolute support and trust in my potential from the beginning to the end of this international journey. I also dedicate it to my girlfriend. She believed in me and my goals, even when we were far away from each other.

My resilience comes entirely from having you in my life. My success and achievements are directly related to the affection and comfort you provide. This is my way of thanking you for everything you make possible.

Acknowledgement

Firstly, I appreciate the collaboration between the CEFET-MG and IPB institutions. It was this collaboration that made my activities in Portugal possible as a double degree student. I am also grateful for the contributions of the CeDRI and CIMO centers in providing materials and resources for scientific exploration. Also, I would like to thank the CNPq for all the support in the project.

I thank my advisor, Professor José Lima, for his integral guidance and contextualization of the CeDRI center. I want to thank Professor Ana Pereira for trusting in my potential and introducing me to iCarbono, the project that also motivated me to do this work. I also thank Murillo Ferreira for his essential guidance on writing scientific texts.

I would also like to thank three professionals of the highest excellence with whom I have had the pleasure of working. Professor João Paulo Castro for introducing me to the environmental field, which I have always been interested in expanding my knowledge. I would also like to thank researchers João Mendes and Vinicius Grilo for their friendship, advice, and top-level expert support.

I am grateful to my family for always being by my side. To my parents, Christiane Duarte and Marcelo Britto, for their good humor, teachings, and unconditional support. I dedicate this to my blood sister, Helena, for seeing in me an example to be followed. I appreciate the concern and support of all the other relatives.

Finally, I would love to thank my girlfriend, Ana Clara Rios, for her constant support and unconditional affection. Apart from her visit, she has always shown great passion and consideration for me. She was clearly committed to me when she agreed to live with me while I was away for a long time, and I am very grateful for that.

"Intelligence is the ability to adapt to change."

Stephen Hawking

Abstract

Growing awareness of environmental impacts is making it more important than ever to explore regions with dense vegetation. Remote monitoring is a viable solution for the surveillance of large areas, such as forests. Based in intelligent systems, this work aims to develop a methodology for assessing carbon sequestration in forest areas. Deep learning (DL) structures were used to predict the heights and stand densities in tree colonies. Light Detection and Ranging (LiDAR) sensor scans obtained by Unmanned Aerial Vehicle (UAV) overflight were processed to extract elevation values and images. Point clouds were processed using QGIS software. The LAStools extension was employed to manipulate Digital Elevation Model (DEM) and rasters, obtaining relevant information. This data was then used to create a dataset for implementation in Convolutional Neural Network (CNN) models. Specific biometric relationships were implemented to estimate additional data such as Above Ground Biomass (AGB) and phytovolume. After evaluating different architectures, the VGG19 CNN model was highlighted as the most promising. An area of 46.6 hectares was covered, with an estimated total value of 4225.81 tons of carbon. This value provided an accuracy of 91%, based on forest inventories carried out in the same region. The study was conducted in the northern region of mainland Portugal, encompassing two distinct *Pinus pinaster* Ait. forests.

Keywords: Carbon sequestration; Forest areas; Convolutional Neural Network; RGB images; QGIS software

Resumo

As preocupações ambientais tornam cada vez mais pertinente a análise de regiões com vegetação densa. A monitorização remota apresenta-se como uma solução viável para a fiscalização de áreas extensas, como as florestas. Este trabalho visa desenvolver uma metodologia inteligente para análise do sequestro de carbono em áreas florestais. Foram utilizadas estruturas de Deep Learning (DL) para previsão das alturas e densidade de cobertura em colónias de árvores. Dados do sensor LiDAR, obtidos por sobrevôo de UAV, foram processados para extração de valores de elevação e imagens. Nuvens de pontos foram processadas no software QGIS que, com o auxílio da extensão LAStools, os dados relevantes foram obtidos por manipulação de DEMs e rasters. Estes dados foram utilizados para se estabelecer um dataset para implementação em modelos de CNN. As relações biométricas específicas foram implementadas para se estimar dados adicionais, como a biomassa acima do solo e o fitovolume. Após a análise de diferentes arquiteturas, o modelo de CNN VGG19 obteve melhor performance. Uma área de 46.6 hectares foi analisada, estimando um valor total de 4225.81 toneladas de carbono. Este valor conferiu uma precisão de 91%, baseado em inventários florestais levantados na mesma região. O estudo foi conduzido na região norte de Portugal continental, abrangendo duas diferentes florestas de *Pinus pinaster* Ait.

Palavras-chave: Sequestro de Carbono; Áreas florestais; Convolutional Neural Network; Imagens RGB, Software QGIS

Contents

List of Tables

List of Figures

Acronyms

R^2 Coefficient of Determination

AGB Above Ground Biomass

AGC Above Ground Carbon

AGV Autonomous Guide Vehicle

CHM Canopy Height Model

CNN Convolutional Neural Network

DBH Diameter at Breast Height

DEM Digital Elevation Model

DL Deep Learning

DSM Digital Surface Model

DTM Digital Terrain Model

LiDAR Light Detection and Ranging

MAE Mean Absolute Error

MLP Multilayer Perceptron

MSE Mean Square Error

QGIS Quantum Geographic Information System

RGB Red, Green, and Blue

RMSE Root Mean Square Error

SD Standard Deviation

TIFF Tagged Image File Format

UAV Unmanned Aerial Vehicle

Chapter 1

Introduction

For decades, environmental impacts have precipitated a series of side effects that directly threaten the population's well-being [1]. Managing and monitoring vegetated areas, including forests, is a potential solution to this global threat. A "forest inventory" is a typical technique to collect forest information for a specific region. The approach entails systematically documenting relevant variables about trees within a designated forest stand, such as total height and Diameter at Breast Height (DBH) [2]. A forest inventory enables the extraction of information related to species colonies from the study region. Consequently, recognizing these regions can be crucial in implementing the appropriate interventions necessary for each distinct scenario.

Despite the advantages of forest inventories in addressing ecological challenges, obtaining such surveys using conventional methods can present significant obstacles. The presence of remote conditions and irregular relief points two recurrent difficulties in this scenario. This scenario poses a direct threat to human safety and the integrity of fieldwork. Consequently, there is a growing demand for alternative methods to circumvent the necessity of field incursions. One potential solution involves implementing Autonomous Guide Vehicles (AGVs), which can function in adverse environments [3]. Furthermore, AGVs possess the capacity to facilitate the transportation of equipment, such as sensors or measuring devices, improving efficiency and safety. Their application advantages support the utilization of AGVs for forest inventory surveys [4].

UAVs are capable of flying over a region, making them a promising contribution to the analysis of hard access areas. This capability enables UAVs to circumvent the challenges typically present in wild environments, such as variations in terrain and stand density [5]. Consequently, using UAVs in field scans can yield substantial advantages, including a notable reduction in operating time, a factor always advantageous [6]. Furthermore, integrating sensors and cameras into UAVs enables comprehensive data collection, facilitating analysis and decision-making processes. This versatility in instrumentation facilitates a range of methodologies for extracting information from forest environments using UAVs [7], [8].

Among the available methodologies for analyzing forest information, the digital representation of the study environment is often highlighted. This approach suggests a reconstruction of the layout of field elements, integrating a substantial volume of information [9]. In many cases, this reproduction process is referred as "point cloud". However, the process is subject to limitations imposed by the parameters of the flight mission, which can result in the loss of crucial information. For example, canopy cover can be a barrier to data extraction at particular height levels. The values stored in a point cloud may deviate from those expected for the target variable. This scenario underscores the necessity of rigorous data processing to ensure the integrity and validity of the results [10].

In the context of substantial datasets, technological resources have the potential to facilitate the manipulation and individual interpretation of each piece of information. Artificial intelligence encompasses a range of approaches, including statistical methods for processing data. These tools are particularly beneficial in scenarios with larger volumes and data varieties, as with point clouds. Among the numerous concepts in this domain, DL has emerged as a particularly salient one [11]. CNN is a subcategory of DL algorithms, predominantly used for image analysis. When implemented effectively, a CNN model can identify patterns within image datasets and extract the desired values from the processed information [12].

1.1 Motivation

As a viable solution for mitigating environmental and climate impacts, controlling carbon sequestration mapping plays a key role. This scenario is a common effort among scientific bodies and government policies. International organizations, such as the Intergovernmental Panel on Climate Change (IPCC), disseminate information regarding the primary causes and potential strategies to overcome the adverse effects associated with these issues [13]. This knowledge is then incorporated into norms, promoting regulative establishments that governments are oriented to adhere to [14].

The European Green Deal (EGD) calls on the European Union member nations to achieve neutrality in their toxic gas emission rates by preserving forest regions, for example [15]. Forest areas monitoring, preceding their carbon stocks, plays a significant socioeconomic interest for governments seeking to regulate or maintain their degradation rates [16]. Thus, implementation of this objective on a large scale, particularly in areas with extensive vegetation cover, is often time-consuming and resource-intensive.

Integrating technological tools with well-fitted theoretical foundations can offer practical solutions to this surveillance case [17]. A functional and practical model can be established upon approving a procedure in terms of its precision in results. Thus, significantly reduced expenses and analysis periods were presented. This strategic plan can be adopted to manage large mainland territory extensions efficiently [18]. Meanwhile, a validated methodology for carbon storage analysis can be employed in other applications with similar analysis requirements. The field of precision agriculture is also encompassed in this monitoring alternative [19].

Furthermore, this work was motivated by the iCarbono project PL23-00038, founded by Fundação La Caixa. In order to access carbon sequestration above ground in forest areas, the work is directly related to the iCarbono objectives. And also, the work contributes significantly to the international cooperation project 442696/2023-0, titled "*Study of Cooperative and Autonomous Inspection in Plantations*", funded by CNPq.

1.2 Objectives

This work proposes an innovative methodology for relevant information extraction from forest areas by CNNs models implementation. The carbon rate, in tons per hectare, will be the final target variable achieved by the technique. Thus, total carbon sequestration in extensive sites aims to be reached. In addition, variables such as volume and biomass measurements will also be covered. Wide data acquisition, processing, and implementation procedures will be conducted to achieve this primary objective.

Raw data (point clouds) obtained by UAV overflight transporting LiDAR sensor, will be processed on Quantum Geographic Information System (QGIS) for relevant information extraction. Accessing elevation values (vegetation height) by DEMs manipulation, Red, Green, and Blue (RGB) images will be appropriately labeled for CNN models implementation. Thus, the total height will be the model prediction output. As model input, a variable linked with the local stand density will also be predicted for each RGB image.

Considering the total height values obtained for each input data, the biometrics relationship will also achieve complementary forest measurements. Specific hypsometric relationships and allometric equations will achieve phytovolume, AGB, and other variables for each test sample. All CNN results will be evaluated considering their respective ground truth values, obtained by a forest inventory survey within the exact location.

1.3 Document Structure

This work was organized into seven chapters, following the Introduction, to provide more comprehensive material.

The second chapter, “State of Art”, presents a collection of already published works with some similarity to this work. Nine different research studies were meticulously explored, achieving a solid background.

The third chapter, “Foundations and Tools”, ranges the theoretical concepts employed in this work, such as all the physical and virtual resources.

The fourth chapter, “Methodology”, describes all steps and definitions carried out aiming to achieve an innovative forest area analysis technique. Furthermore, the best-suited model are also established.

The fifth chapter, “Case Study”, presents an isolated application case, along with its relevant information, to be applied to the developed methodology.

The sixth chapter, “Results and Discussion”, shows all the obtained results followed by their discussion. It is divided into two sections, each related to a specific case study.

The last chapter, “Conclusion and Future Works”, summarizes the technique developed within its focal results achieved. In addition, some research continuation proposals and already published works related to this work are highlighted.

Chapter 2

State of Art

The ability of plant species to absorb Carbon Dioxide (CO_2) renders the vegetation a pivotal role in the carbon cycle, particularly in regulating its concentrations in the atmosphere. According to [20], terrestrial ecosystems can neutralize approximately 11.2 *Giga tons* of CO_2 per year. This statistic indicates that approximately 29% of anthropogenic CO_2 emissions are neutralized, with forests exhibiting a notable capacity to serve as the primary sinks for the gas. The persistent challenges posed by unsustainable land use and ongoing climate change have led to a decline in forest cover.

However, pertinent analyses had already been published, providing essential considerations regarding the carbon-neutralization scenario. A temporal study revealed a substantial increase in carbon emission rates due to improper land use from 1850 to 2015. It was highlighted that tropical forest regions were primarily impacted by anthropogenic activity. Situated areas at higher latitudes, including the temperate and boreal zones, have assumed a significant role as sinks, thus compensating for these observed gaps [21].

Despite the environmental complications, the study [22] demonstrated that forest regions continued to sequester carbon on significant scales. It has been indicated that precise biomass estimation is paramount for ensuring the long-term storage of carbon and for the mitigation and neutralization of gas. However, the utilization of technological resources in monitoring forest regions was outlined to maintain the most excellent possible integrity of the global forest sink [22].

Employing artificial intelligence techniques, the research [23] provided an accessible solution for remote monitoring of tropical forests. The motivation for the study was the emergence of government policies aimed at mitigating deforestation and the misuse of plant resources. Satellite images with a resolution of $30 \times 30m$ were used to cover extensive swaths of land. To train learning algorithms to predict carbon stocks in the interest plots, LiDAR data was also used. The resulting dataset incorporated satellite images and LiDAR overflight elevation values.

To overcome the limitations of extracting details from satellite images by the study [24], the researcher used high-precision LiDAR scans, which were obtained through UAV airborne surveys. A comprehensive analysis was conducted to examine the recognition of patterns in images, thereby enabling the implementation of machine learning structures. Additionally, the DEMs of the study regions were generated, thereby extracting local information of interest. In light of the observed parallels with the research [23], field surveys were also conducted to parameterize and validate the variables and results obtained by machine learning.

The work [25] investigated the accuracy and reliability of LiDAR data obtained through Aerial Laser Scanner (ALS), a widely used remote forestry analysis technique. During the study, various DEMs were produced by classifying points within LiDAR point clouds. The "*las2dem*" tool, which is part of the LAStools library, was used to generate Digital Terrain Models (DTMs), Digital Surface Models (DSMs), and Canopy Height Models (CHMs) for the designated study regions. Because this is a low-density LiDAR scan provided by ALS, data processing inconsistencies have been reported. The primary challenges encountered included the difficulty of identifying smaller trees and the presence of dominant trees at a lower canopy level. Correction errors were applied to the DEMs to optimize the results, while dominated trees were disregarded.

The conducted study [18] investigated the carbon neutralization of forest cover by analyzing satellite images. Deep learning architectures were implemented to achieve this goal, with satellite images designated as the input data. The photos were labeled according to field data obtained in specific locations of the Chinese forests under investigation.

Implementing the CNN models achieved the most optimal results. A comprehensive evaluation of the available models was conducted, and the AGB and carbon density indices were mapped through prediction, exhibiting favorable coefficients of determination (R^2).

In line with the promotion of remote monitoring of carbon stocks, the work [17] attempted to publish labeled data sets from RGB overflight images from UAVs. The labeled values for carbon stocks were obtained through allometric equations, with field data serving as ground truth. The study incorporated a complete carbon analysis within the plots of interest. The trees contained in each image were identified using algorithms during data processing. A CNN model, ResNet18, was employed to predict individual AGB values according to the crown characteristics of each individual. A total of six datasets of labeled RGB images were made available, as the analysis of the field data revealed similarities with the predicted results of the algorithm.

In [26] possibilities for crown delimitation in mangrove colonies of different stand densities using UAV-based LiDAR scans were explored. Relevant data, such as height, volume, and crown structure, were assessed using DEMs. Despite the greater complexities associated with higher stand densities, the study proved feasible for applications such as monitoring carbon sequestration. Of the 126 mangroves analyzed, 46% had their canopies properly segmented. This was achieved using the variable window filtering method and the marker-controlled watershed segmentation algorithm.

The study [27] investigated the segmentation of tree canopy and the identification of their structures and species. Accurate results were obtained by applying machine learning algorithms like Random Forest. A total of 18 species were identified using UAV-based LiDAR scanning data and ultrahigh-resolution RGB and hyperspectral imagery. Access to DEMs, such as CHM, enables canopy delimitation and species identification to provide essential insights into estimates such as carbon sequestration in mixed populations.

Beyond the context of forestry analysis, similar remote monitoring approaches can also be applied in precision agriculture scenarios. The research [19] employed UAV-based LiDAR scans to conduct a study that analyzed biomass in onion plantations. The estimation of biomass in plantations at distinct growth stages was facilitated by using

point clouds and DEMs. The RGB models were processed within the VOL_LAIC software using the LAStools extension. The target variables for predicting biomass from RGB imagery were green canopy cover, crop height, and canopy volume.

Finally, new methodologies can be established mixing some technologies and approaches as previously highlighted. The use of LiDAR data from UAV overflights suggests an acquisition approach with wide frameworks to explore, which encourages the implementation of prediction algorithms. Available in the QGIS software for example, the LAStools extension offers essential resources for processing point clouds, generating rasters or DEMs. Once local imagery and its respective elevation values (tree heights, considering a forest environment), a robust model can be achieved to access complementary and more significant variables from the study site, such as carbon sequestration rates.

Chapter 3

Foundations and Tools

This chapter presents a bibliography review, which encompasses the concepts adopted during the study. A selection of previously completed works about forest inventory analyses and UAV scanning is also showcased. The section ends with a brief description of the employed equipment, virtual environments, and methods.

3.1 Theoretical Background

This section presents an overview of the theoretical ideologies related to the topics covered in this work. The objective is to establish a consolidated theoretical base for fluid interpretation of the concepts and technologies used in the study.

3.1.1 Unmanned Aerial Vehicle

Traditionally related by drones, UAVs are an autonomous vehicle category with significant, efficient, and adaptable characteristics, attributed to their ability to hover precisely [8]. Because of their high versatility, this technology presence is growing fast in a large variety of applications, such as precision agriculture [28], thermal inspection [29], and complex accessing areas data collection [30].

With many advantages, UAV is a key technology for simplifying many human tasks,

obtaining satisfactory results, and significantly reducing the operation time. On the same page, some applications offer health risks, making it preferable to use UAV to overcome them [31]. Employing UAVs is also advantageous in scenarios where the target site analysis exhibits accessing complexities, such as topography, aquatic areas, disaster-stricken regions, battlefields, etc.

The fast growth of application possibilities and popularity of UAVs influenced the surging of various configurations. Suspension capacity, flight speed, propellers number, structural dimensions, and hardiness, are some of the diversity specifications attributed to each exemplar. Following this, it is suggestive that the UAV model becomes selected based on the application predestinated to operate [31].

3.1.2 Light Detection And Ranging

FLight Detection and Ranging (LiDAR) is a scanning technology that aims to represent an environment by combining distance measurements between the sensor and objects, or surfaces [32]. Typically, each distance value is obtained by one or more laser beams, oriented by the LiDAR system field of view. The difference within the same direction between the signal transmitted by the laser pulse and received by the photo detector results in the range detected [33].

Distance measurement can be achieved using diverse calculation approaches. One such method is Time of Flight (ToF), which involves measuring the distance based on the travel time interval obtained by a signal from a source to a target [33]. The signal emitted is immediately reflected upon contact with an obstruction and subsequently captured by the photo detector. The distance traversed value is calculated according to this dynamic process, as illustrated in Fig. 3.1.

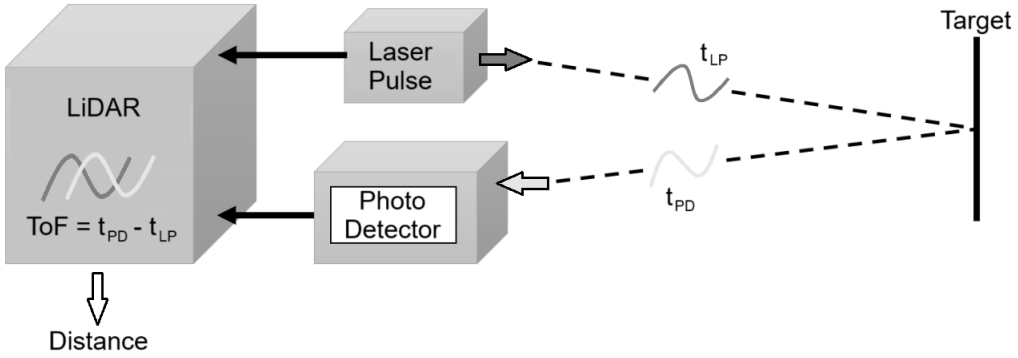

Figure 3.1: Time of flight dynamic for distance measurement in LiDAR devices. Source: Adapted from [33].

A LiDAR sensor can generate an environment representation in one, two, or three dimensions. Some of its configuration defines the operation dimension, such as scanning inclination and angle movement [32]. The choice of the scanning dimension varies according to each application. So, considering the environment representation complexity, the LiDAR model must be defined.

A digital reconstruction can be more detailed, changing the LiDAR relative position during an environment scanning LiDAR. This is also an efficient approach for complex representations. Minimizing the loss of information for overlapping, an extended area can be represented with satisfactory precision [4].

An UAV can be employed as a transporter of the LiDAR sensor during an environmental scan. This set is typically named by UAV-based LiDAR [26], [27]. Considering the large gap for both technology applications, this approach is increasingly applied to tasks that require high displacement versatility and detailed precision. To clarify the term, Figure 3.2 shows the UAV-based LiDAR employed in this study.

Figure 3.2: UAV-based LiDAR set employed in this study (M300 RTK + L1 Zenmuse).

3.1.3 Point Cloud

The term point cloud refers to a group of points with three-dimensional coordinates in a single spatial ambient. Generally, a point cloud generation is based on a significant points dataset, which implies a trustworthy real environment representation [34]. Each point usually has additional parameter values beyond the axis displacements. Plus, information depends on the extraction device, possibly bringing key variables to the case study, such as color and georeferencing [35].

Moreover, a point cloud can be converted into different displacement models, such as pixel grade. This approach imports the information the point cloud gives, saving each pixel with its respective data value. This representation is typically mentioned in the literature as raster [36]. Condensing the information, a rasterized point cloud can offer some advantages, mainly considering digital representation processing.

3.1.4 Digital Elevation Models

Digital Elevation Models (DEMs) are representations in which each cell has a corresponding height value about sea level. These units are typically labeled using geographical

coordinate systems. This factor set implies that DEMs are relevant resources in geospatial and cartographic studies [36].

Many categories of DEM exist, each meticulously designed to represent specific elements within a designated environment. The Digital Terrain Model (DTM) and Digital Surface Model (DSM) represent two types of DEMs that have been extensively explored in the extant literature [36]. The DTM aims to depict the soil profile of a given region, disregarding elements such as buildings, transmission lines, and vegetation. The DSM encompasses all visible, or above-ground, environmental elements. Figure 3.3 shows a facilitated comparison between their concepts.

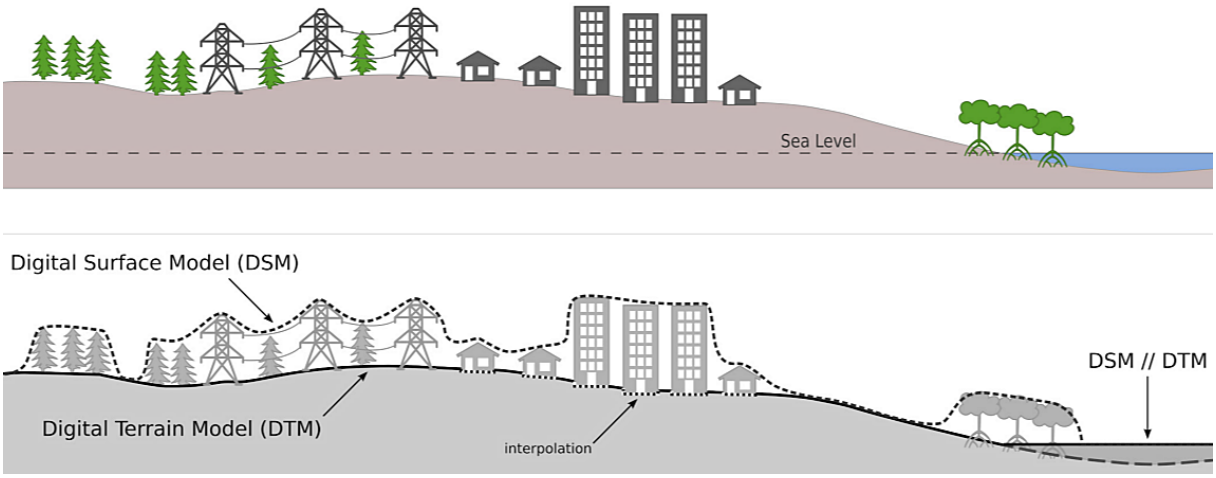

Figure 3.3: Difference between encompassed elements by a DTM and DSM.
Source: Adapted from [36].

Alternative DEM models can also be achieved by interacting with different typologies. The CHM is a valuable tool for environmental and land use analysis, and it can be obtained by differencing the DSM and the DTM [37]. By representing tree heights and canopy cover, the CHM offers essential properties for forestry analysis [38]. The selection of the appropriate DEM is contingent upon the particulars of the case study.

The data accuracy represented by a DEM is associated with different causes. The

resolution of the acquisition device, elevation correction, and errors associated with data processing are some of the key factors that affect the reliability of a DEM [39]. The application of statistical methods facilitates the diagnostics of error accumulations and their effects.

DEMs can be obtained using different acquisition methods. Using airborne LiDAR by UAVs constitutes one of the most highly accurate acquisition approaches. When the sensor is positioned near the scanning environment, it is possible to obtain multiple pulse readings, thus enhancing the precision of the measurement [37], [38]. Using satellites has emerged as a particularly salient solution, primarily focusing on acquiring coverage [18], [23]. By contrast, the distance from the target environment and its elements implies a substantial resolution decrease.

3.1.5 Biometric Relationships

It is imperative to note that variables associated with forest environments and their direct correlations with each other offer substantial insights into the assessment of tree volume, biomass, and carbon storage within the designated area [2]. The primary objective of field data collection is to acquire fundamental information, including diameters and heights [40]. Employing specialized equipment, such as calipers and hypsometers, enables the precise documentation of forest parameters, thereby ensuring the accuracy of the recorded values [41]. Consequently, the collection of measurements with minimal error potential should be prioritized whenever feasible. Directly associated with total height, the DBH is an emphasized reference point for forest inventories [2]. The relationship between DBH and total height is delineated through hypsometric equations [41].

In addition to the diameter-height relationship obtained using hypsometric equations, allometric equations provide essential complementary information for forest inventory research. Volume, biomass, and carbon stocks are the main variables that can be estimated using these equations [42]. Thus, allometric equations represent an often-used method for obtaining relevant information in forest inventories [43].

However, biomass calculation is often executed with caution, particularly due to its relationship with market values or the quantification of carbon stocks [43]. When applied to allometric equations, this calculation tends to be accurate, with minor deviations from actual values. Nevertheless, these deviations can be minimized by employing specific allometric equations for a given plant species, eschewing generic models [44].

As well as hypsometric diameter-height relationships, applying allometric equations is beneficial when validating or complementing datasets. In the context of forest surveys, it is common to observe strategies that facilitate the reliable analysis of the environment. The Draudt method is founded on the principle of acquiring only the most accessible variables in the field [45].

The technique outlines a zone delimitation within the total area of the analysed forest. The trees within the investigation zone are classified according to their DBH values. Considering $5cm$ intervals ranking, for each band, the tree with the highest DBH is classified as dominant and separated into groups of five individuals. The first tree that exceeds the group within a DBH range is classified as a sample. Additional measurements, such as total height and cross diameter, are extracted only from dominant and sample trees. However, Draudt's method assumes that investigating the delimited zone provides a reliable representation of the entire study region [45].

The application of allometric equations, under the assumption that total heights and DBHs values are obtained directly from the study sites, is a plausible approach. The availability of information such as phytovolume, AGB, and carbon sequestration facilitates a more comprehensive generalization of the region of interest [42]. Applying biometric relationships to other forest analysis contexts, such as DEMs, is also possible. Given that CHMs contain the respective tree height values, their diameters can be accessed by employing the species hypsometric relationship [25]. Furthermore, with height and diameter values, allometric equations can also be applied.

3.1.6 Deep Learning

Deep Learning (DL) is an artificial intelligence technique that aims to allow machines to extract and interpret patterns from data. This approach is predicated on a hierarchy of concepts, whereby a set of simpler characteristics represents each piece of information [12]. To break down raw data into more interpretable information, DL algorithms are structured in layers, such as the Multilayer Perceptron (MLP) architecture. The layers of a MLP are based on mathematical models that describe the characteristics of a piece of information in terms of input and output values [46].

In addition, the amount of data used to train an DL algorithm is directly related to the accuracy of its final results. A larger amount of data, possibly with slight differences, allows the algorithm to be more adaptable and perform better. It is therefore reasonable to always have a moderate size for the network's training and validation dataset [46].

It is evident that, when a DL structure is employed in conjunction with a meticulously designed dataset, the algorithm can prove to be highly efficacious in the extraction of information from raw data [47]. This is because slight variations in the input data do not typically hinder the trained network from yielding satisfactory results. Consequently, it is imperative to undertake an extensive training and validation phase to ensure the attainment of optimal outcomes [48]. Typically, the implementation of learning platforms, such as DL, is based on the following separation of stages:

- **Training**: This stage involves the identification of patterns between raw input data and labeled values. It typically generates the largest volume of input data for establishing relevant patterns;

- **Validation**: Following the assimilation of patterns by the model, an analysis of the learning performance of its parameters is undertaken to obtain more stable results, thus avoiding the outcomes of under- or over-fitting;

- **Testing**: A portion of the data is employed to evaluate the performance of the configured structure. For a more comprehensive evaluation, the testing data is

generally separated from the training and validation data and is unknown to the trained network.

3.1.7 Convolutional Neural Network

The term Convolutional Neural Network (CNN) is used for neural networks that have the mathematical operation of *convolution* in at least one of their layers [49]. Due to their layered architecture, CNNs are classified as a subcategory of DL [46]. CNNs are typically used for applications with a more concrete input data layout. This is evidenced by their frequent application in image analysis, a field such as computer vision. The fixed 2D data structure, which considers the arrangement of pixels in an image, provides a suitable scenario for applying the convolution layers of a CNN [50]. This allows for a more precise extraction of relevant information in an image that can usually present the same element differently.

The diverse layer settings of a CNN engender various structures for information extraction. Some established groups, such as Visual Geometry Group, Residual Networks, Mobile Nets, and Efficient Nets, present a well-structured architecture that generally yields favorable results [51]–[54]. The peculiarities of these models will be discussed further in Section 3.2.3.

Following the division of the traditional learning process into stages, the *k-Fold Cross Validation* methodology offers an efficient approach to generalizing the trained network. The technique involves splitting the amount of input data (dataset) into k sets. Each split set is applied in a specific learning phase [46], [55].

The sets are used for training and validating, ensuring a comprehensive evaluation of the trained network. In each iteration of the process, one of the sets is designated for validation, while the remaining sets are employed for training. This procedure is repeated until each set has been used for validation at least once. The final evaluation of the model parameters is based on the contribution of all k sets [55]. Figure 3.4 shows a typical dataset splitting and configuration by *k-Fold Cross Validation* implementation for

training and validation phases.

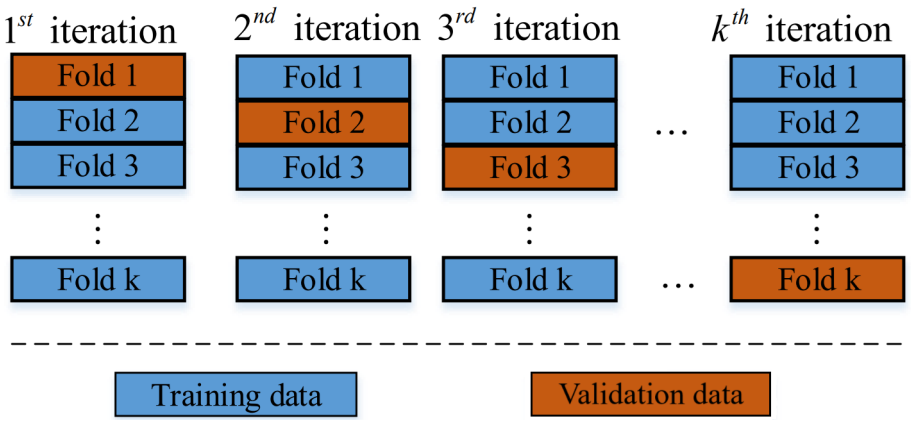

Figure 3.4: *k-Fold Cross Validation* implementation.

Source: Adapted from [55].

The implementation of *k-Fold Cross Validation* is particularly advantageous in cases where there is no larger volume dataset with minimal differences between the labels of the input data [46]. By employing this technique, the training and validation stages become less susceptible to bias caused by similarities in the data, thereby reducing the likelihood that the trained network will perform well simply because of how the data have been divided.

3.2 Materials, Virtual Resources, and Methodologies

This section will present this study's primary physical, virtual, and scientific resources. The measurement and technological equipment, data processing software, CNN structures, methodologies, and evaluation metrics will be delineated.

3.2.1 Equipments and Devices

The representative equipment and devices used in the research will be delineated. This includes both the field and scanning stages.

- **MATRICE 300 RTK UAV**

  Provided by DJI Enterprises, the MATRICE 300 RTK (Figure 3.2) is a hovering technology platform that is characterized by high precision and safety. The drone has an integrated Real Time Kinematic (RTK) module, which provides constant georeferencing updates. Its dual Inertial Measurement Units (IMU) and barometers design ensures flight precision, enabling measurements with centimeter accuracy about the established reference [56]. The collaborative operation of the RTK module, the IMUs, and the Global Navigation Satellite System (GNSS) enhances the model's reliability.

  Its versatility is further advantageous for applications that require a high level of detail, such as mapping urban perimeters or forestry areas [57]. The model's design, which supports dual power supply batteries and an extended data transmission range, renders it suitable for operations across various scenarios, including those within irregular topography. Furthermore, the drone's advanced sensing and safety protocols enable its operation in confined environments, such as tunnel inspections, ensuring its versatility and reliability in various applications [58].

- **Zenmuse Li LiDAR**

  Also supplied by DJI Enterprises, the L1 Zenmuse device, shown in Figure 3.5, was developed to work with the M300 RTK aircraft. Its configuration consists of a LiDAR module, an IMU, and an RGB mapping camera [59].

  The acquisition of richer point clouds, including height, RGB, distance, and reflectivity values for each point, can be achieved by configuring flight missions through the DJI Pilot app. This feature positions the L1 Zenmuse device as a valuable resource for the reconstruction of complex environments through the use of point clouds with a substantial volume of colored points [60].

- **LT800**

  The LT800 is a robust meter-level positioning device ideal for applications requiring

Figure 3.5: DJI L1 Zenmuse device.

portability and precision. Supporting GPS, GLONASS, Galileo, BeiDou, QZSS, and SBAS, it presents whole constellation GNSS positioning [61]. However, the LT800 is particularly well-suited for challenging applications, such as coastal zone management, forest mapping, and wildlife tracking [62].

- **Haglöf Sweden Mantax Blue Caliper**

  Haglöf Sweden's catalogue of calipers encompasses a wide range of product categories, including the Mantax Blue, a non-electronic model. This line of equipment is fabricated from highly durable materials, including alloy-coated non-reflective aluminium and armoured glass fibre polycarbonate plastic. The measurement printings are of high quality and meticulously applied, with the option of customized units available upon request. The equipment is notable for its wide range of scales, allowing it to be used in various applications, including forest inventories, wildlife management, construction, healthcare, archaeology, and geology [63].

- **Haglöf Sweden Vertéx 5**

  The Vertéx 5, developed by Haglöf Sweden, is a practical and highly reliable solution for measuring tree heights. The device has a resolution of $0.01m$ and an accuracy of

1% or more, provided if properly calibrated. The device exhibits a measuring range of up to 999 meters, thereby classifying it as a high-performance tool, particularly well-suited for medium-height trees [64].

The Vertéx 5 can be used with a transponder to ensure dependability in practical applications. The kit was initially accompanied by the T3 Transponder, which the T4 version has since replaced. This change has resulted in technical specifications that are more aligned with current demands.

The device has an intuitive interface that facilitates the configuration, calibration, and measurement processes. Haglöf Sweden provides detailed, illustrated instructions for each procedure, facilitating comprehension and utilization of the equipment [65].

- **Mattson Increment Borer**

  The increment borer, initially developed by the German inventor Pressler in 1889, has undergone various modifications and improvements in its production process. Haglöf Sweden exerts a dominant influence over the increment borers production market, offering a range of products that encompasses the classic Mattson and Djos models, in addition to its brand.

  Mattson borers are characterized by their robust construction, which includes brass handles and a chemical coating of phosphorus and nickel. This coating serves to enhance the borer resistance to corrosion. The drill tip features a convex arc shape, which is ideally suited for precise sample extraction. Various drill diameters and lengths are available, directly reflecting the proportions of the sample to be extracted [66].

3.2.2 Virtual Environments

DJI Terra is a virtual environment that facilitates the precise and efficient reconstruction of two-dimensional (2D) and three-dimensional (3D) models. The software enables

the representation of scenarios characterized by vertical elements, including forests and power transmission lines. Photogrammetry is the primary tool employed in this process, generating optimal conditions for processing data captured by DJI devices, such as the Zenmuse series [67].

Before processing scan data, such as LiDAR data, DJI Terra also enables flight planning. The precision of a scan can be enhanced by meticulously designating its points of interest or delimitation. The software provides digital maps, or orthomosaics, for configuring flight and scan parameters on the fly.

Following an environment scan, the data can be processed, generating a file containing all pertinent information in a concatenated format. Consequently, DJI Terra can create a point cloud, which is stored in a ".las" file format. Point classification also facilitates the generation of DEMs in 2D format directly from DJI Terra.

Quantum Geographic Information System (QGIS) is a free and open-source software that allows users to manipulate and analyze 2D representations, including maps and rasters [68]. The virtual environment provides various tools for different functions, such as editing, segmentation, and concatenation. The software also facilitates georeferenced analysis, allowing a real-time coordinate work interface. Its logo is presented in Figure 3.6:

Figure 3.6: Quantum Geographic Information System logo.
Source: [68].

QGIS offers a user-friendly interface, rendering it accessible to beginners and experts in cartography alike. The software also offers versatility, making it possible to import extensions that extend the range of possibilities for cartographic analysis [69]. Applying extensions such as LASTools provides the software with additional tools for manipulating

point clouds stored in ".las" format files.

Developed by Rapidlasso [70], the LAStools collection provides a set of useful tools for processing point clouds. Each tool is described by a robust algorithm, providing a reliable solution for processing LiDAR data. This technology's wide range of applications is demonstrated by its use in diverse fields, including academic, industrial, and governmental domains.

While some tools are free and open-source, it should be noted that specific options have performance restrictions. For example, the "*las2dem*" tool is limited to clean processing point clouds with a point density greater than 1.5 million points. As shown in Figure 3.7, random watermarks are applied for files that exceed this threshold.

Figure 3.7: Above 1.5 million points LiDAR data watermarks insertion on QGIS.

3.2.3 CNNs Algorithm Structures

The rise of CNN architectures has been progressively propelled, emerging as a pivotal element in advancing computer vision. The development of increasing efficiency and complexity in structures has led to the creation of diverse layers with varied numbers and purposes. It is essential to acknowledge the wide range of possibilities for configuring these layers, which suggests a broad range of purposes depending on the typology of each

CNN.

The Visual Geometric Group (VGG) family, proposed in [51], introduced the use of 3×3 filters along the convolutional layers. The selection of this dimension was intended to encompass left/right, up/down, and center displacements, thereby facilitating the establishment of more efficient networks. The VGG16 and VGG19 models demonstrated comparable performance, yet VGG19 was distinguished by incorporating three additional convolutional layers. Despite the satisfactory accuracy of the experiments, the high number of parameters in these architectures implies high computational demands.

Given the complexity, defined by the large number of floating point operations (FLOPs) characteristic of VGG architectures, the research [52] proposed the ResNet family, thereby introducing the concept of residual learning. The authors proposed incorporating stacked residual units to avoid issues related to vanishing and exploding gradients, which reemerge after a specific depth in a network. This approach was subsequently adopted, with the implementation of shortcuts based on the premise that optimizing the residual mapping of each layer would be a more viable undertaking than optimizing its original mapping. To optimize the ResNet50 model, which consists of 50 convolutional layers, [71] proposed the ResNet152V2 topology. In contrast, the new structure implemented batch normalization before each weight layer, thereby ensuring the stability of the training process in even more complex networks.

To apply CNNs to mobile and embedded platforms, which are characterized by more limited processing capabilities, [53] proposed the MobileNet family. This configuration was developed to adapt to the user's needs, allowing for adjustments to hyperparameters and achieving a balance between precision and latency. However, compared to more robust architectures, MobileNets tend to exhibit lower performance metrics. To enhance the efficacy of this family of models, [72] introduced MobileNetV2, a model that incorporates modules for inverted residuals and linear bottlenecks. This enhancement proved pivotal in recognizing MobileNet, particularly within systems characterized by constrained resources.

As demonstrated by [54], the EfficientNet family emerged as a more versatile architecture in terms of the configuration of convolutional layers. The proposed approach entailed the collaborative balancing of input depth, width, and resolution through a composite coefficient, thereby avoiding arbitrary decisions. EfficientNets are distinguished by incorporating mobile inverted bottleneck convolution blocks and the squeeze-and-excitation mechanism designed to enhance pattern channel quality. Starting with EfficientNet-B0, the sequence of models reached its peak performance with EfficientNet-B7, consolidating its position as one of the most efficient CNN architectures at the moment.

Although these architectures have standard input resolutions of 224×224 pixels and 600×600 pixels in the case of EfficientNet-B7, they are also compatible with smaller images. Tests with resolutions of 64×64 and 32×32 pixels for VGG16, ResNet50, MobileNetV2, and EfficientNet were analyzed, observing more significant performance losses in deeper structures such as VGG16 and ResNet50 [73].

3.2.4 Evaluating Metrics

Evaluation metrics are fundamental in applications based on the optimal performance of mathematical models. However, evaluating case outcomes through using several metrics is a reliable approach to ensuring the validation of the research findings. Based on statistical foundations, described in [74] and [75], the following evaluation metrics will be applied in this work:

- **Standard Deviation (SD)**

$$SD = \sqrt{\frac{1}{N-1}\sum_{i=1}^{N}(x_i - \overline{x})^2}, \tag{3.1}$$

where SD is the Standard Deviation, i the observed value index, N the amount of samples, x_i the observed sample value, and $\overline{x}$ the average between sample values.

- **Mean Absolute Error (MAE)**

$$MAE = \frac{1}{n}\sum_{i=1}^{n}|y_i - \widehat{y}_i|, \tag{3.2}$$

where MAE is the Mean Absolute Error, n the amount of comparisons, y_i the ground truth value, and $\widehat{y}_i$ is the predicted value.

- **Mean Square Error (MSE)**

$$MSE = \frac{1}{n}\sum_{i=1}^{n}(y_i - \widehat{y}_i)^2, \tag{3.3}$$

where MSE is the Mean Square Error.

- **Root Mean Square Error (RMSE)**

$$RMSE = \sqrt{\frac{1}{n}\sum_{i=1}^{n}(y_i - \widehat{y}_i)^2}, \tag{3.4}$$

where $RMSE$ is the Root Mean Square Error.

- **Coefficient of Determination (R^2)**

$$R^2 = 1 - \frac{\sum_{i=1}^{n}(y_i - \widehat{y}_i)^2}{\sum_{i=1}^{n}(y_i - \overline{y_i})^2}, \tag{3.5}$$

where R^2 is the Coefficient of Determination, and $\overline{y_i}$ the average between ground truth values.

Chapter 4

Methodology

This chapter provides a detailed description of the steps taken during this study. It also discusses the study's specifics and limitations, offering an initial foray into the proposed subject matter. It will outline the selected study environment, data acquisition and processing, database definition, and the implementation of DL algorithms.

4.1 Study Site

The study was conducted in Terras de Trás-os-Montes, a region in the northern part of mainland Portugal. As illustrated in Figure 4.1, the specific study site was located near the council of Vimioso, in the village of São Joanico. The geographical coordinates of the study region are $41°09'40.4''$ to $41°36'14.7''N$ and $7°47'27.6''$ to $6°27'19.3''W$.

By the Köppen classification, the climate in mainland Portugal is divided into two distinct climate zones, namely Csa and Csb [76]. Within the geographical region of Terras de Trás-os-Montes, the climate is predominantly Csb, described as temperate, with rainy winters and dry, slightly hot summers [77]. The annual mean temperature is 12 to $13°C$, with a yearly precipitation of 600 to $1000mm$.

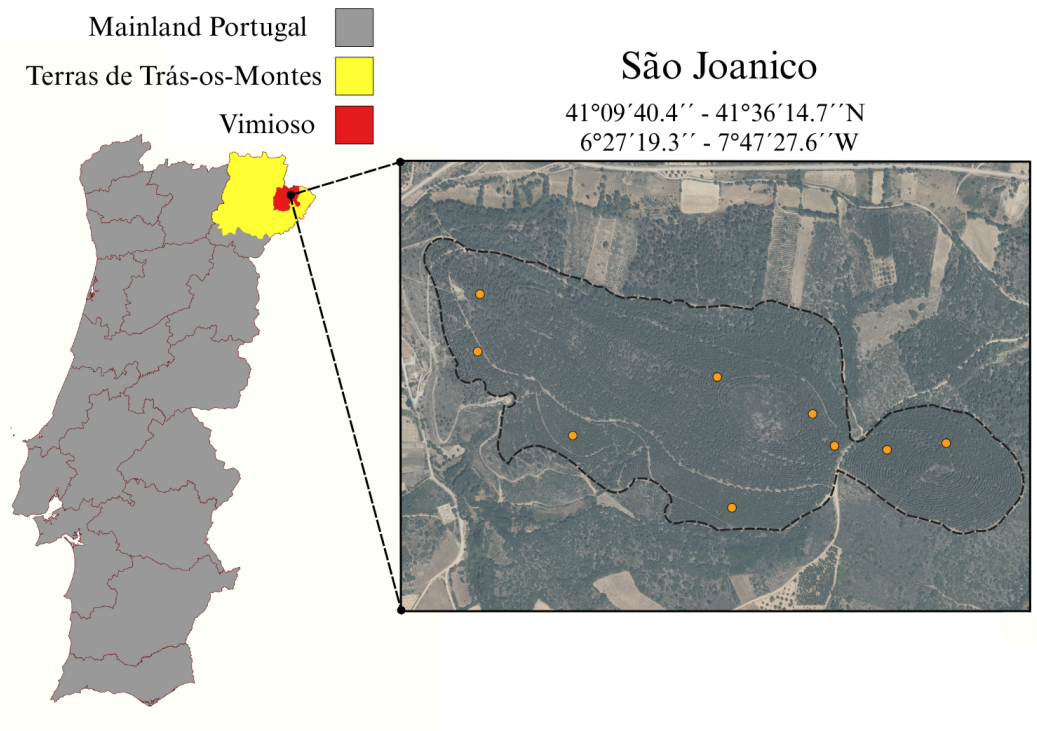

Figure 4.1: São Joanico study site location.

The prevailing species in this region are better adapted to the temperate Mediterranean climate and uneven terrain, such as oaks and pines [78], [79]. *Quercus pyrenaica* Willd. and *Pinus pinaster* Ait. represent large areas of recurrence in the region. As published by [80], the Terras de Trás-os-Montes region presented estimates of 20.3 and 17.2% for oaks and *Pinus pinaster* Ait. vegetation cover, respectively.

Given its more worldwide distribution, reflecting a better extension of horizons, the species *Pinus pinaster* Ait. was chosen for analysis in this study [81], [82]. The oak species *Quercus pirenayca* Willd had already been explored during the work [83]. Furthermore, a comparative analysis of the two species was conducted in [84] in the surroundings of the study site, highlighting the higher concentration of carbon in the *Pinus pinaster* samples, which is the same variable of interest in this study.

The species *Pinus pinaster* Aiton is commonly designated as "*maritime pine*", a designation attributable to its predominance in Mediterranean and temperate regions [82],

[85]. It encompasses medium to high density, typically from 461 to 660$kg.m^{-3}$[85]–[87]. Its characteristics are conducive to economically viable forestry practices, enhancing its vegetative proportions [85], [88].

It is notable for its strong light-dependent characteristic, contributing to predation among its individuals [81]. This dynamic promotes constant competition for sunlight within a colony. Consequently, the density of the species tends to decrease significantly with age progression, with only the tallest trees surviving.

Figure 4.2: *Pinus pinaster* Ait. colony in São Joanico.

Figure 4.2 presents a visual representation of a *Pinus pinaster* Ait. colony situated in the village of São Joanico. On the left side of Figure 4.2, two dominant individuals can be seen, due to the competition of the colony for sunlight. The distinguishing characteristics of these individuals include their notably smaller size and the absence of leaves.

4.2 Data Acquisition

This section will describe the procedures carried out during the data collection used in the study. The research information was extracted in the field and by UAV scans, restricted to the same study environments. Figure 4.3 illustrates a comprehensive schematic of the data acquisition stage.

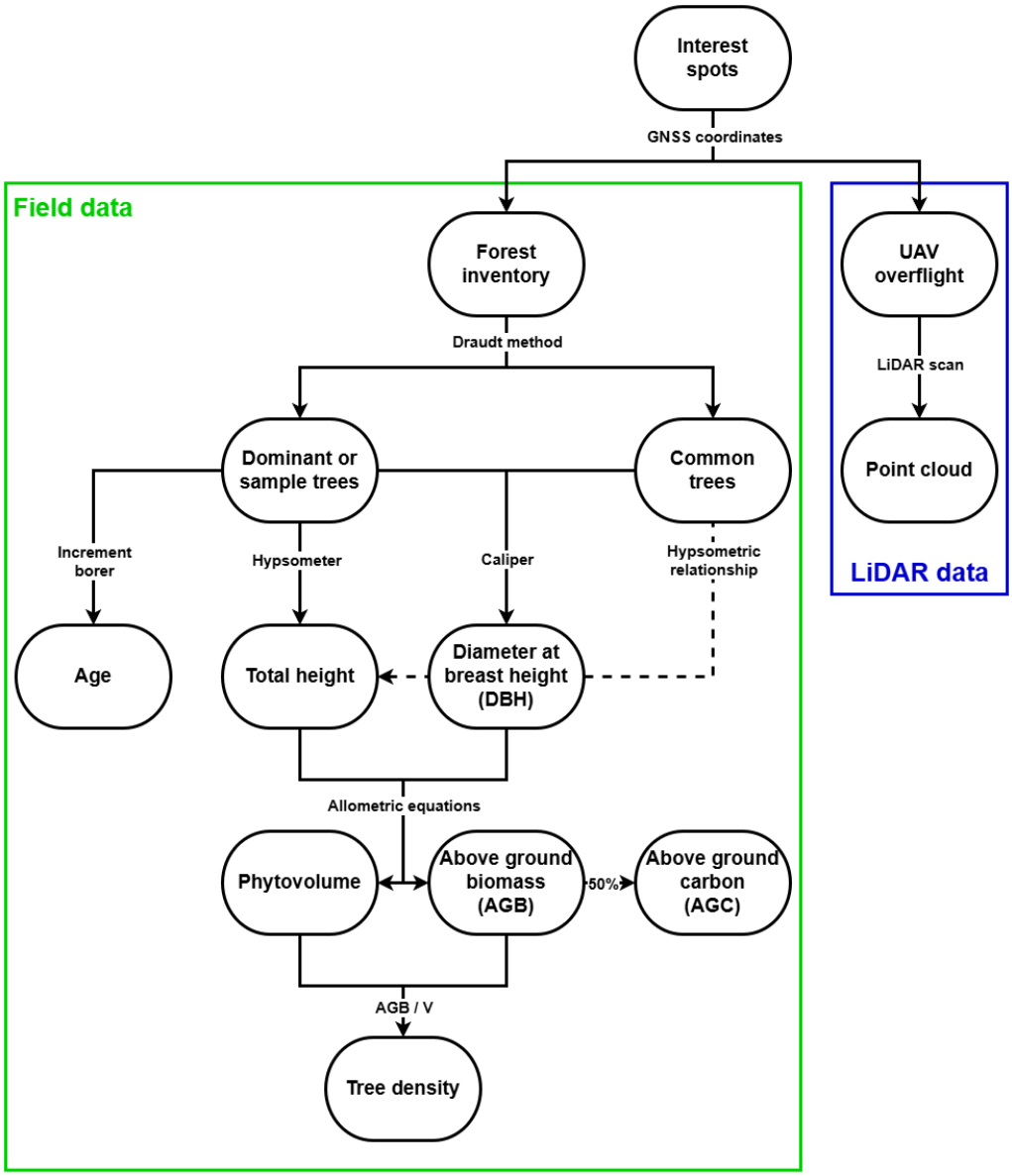

Figure 4.3: Data acquisition schematic.

All the contents illustrated in Figure 4.3 will be described in their respective sections, identified by the same key words. To quickly locate some of the more specific content: “Dominant or sample trees” and “Common trees” classification is described in Section 3.1.5; “Age” was obtained by growth rings analyzes (Figure 4.6); “Total height” and “Diameter at breast height (DBH)” were manually obtained by the procedures showed in Figure 4.5; “Phytovolume”, “Above ground biomass (AGB)”, “Tree density”, and “Above ground carbon (AGC)” were accessed respectively by Equations (4.2), (4.7), (4.8), and (4.9); one example of obtained “Point cloud” is showed in Figure 4.7.

4.2.1 Field data

Field data was collected through manually recorded forest inventory surveys, as contextualized by Figure 4.4. Given the substantial number of target elements (*Pinus pinaster* individuals, in this case), the field study was based on the Draudt method [89]. This approach was implemented to streamline field data collection at the plots of interest.

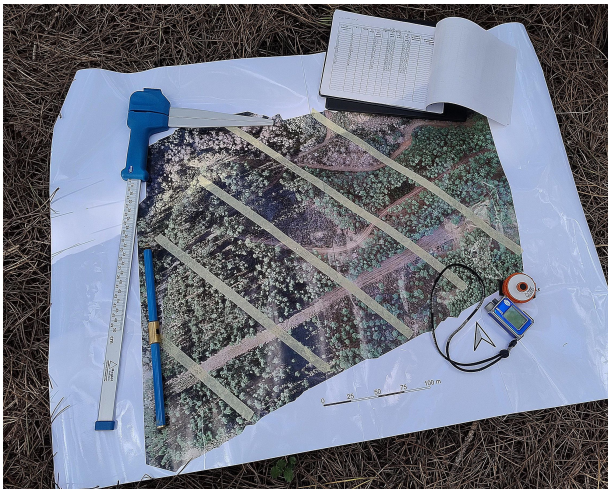

Figure 4.4: Instruments employed in the forest inventory surveys.

The field study covered an effective area of $2250m^2$ by defining a circular area of approximately $250m^2$ for nine different spots. The geographical location of each one was meticulously delineated using an LT800 GNSS [61]. Figure 4.1 highlights each location

referenced by plot centering. The *Pinus pinaster* Ait. Forest area is also depicted, considering a total extension of approximately $40ha$ (obtained on QGIS software).

In the context of carbon sequestration analysis, only information relevant to calculating biomass was considered. However, the forestry variables explored in this study were DBHs and total heights [90]. The pertinent information from the forest inventory was collected in its totality on March 25, 2024.

By the principles established by the Draudt method, reference trees were selected within each of the nine boundaries. Their physical characteristics determined the classification of these trees as dominant or sample. Individuals not included in these categories were identified as common trees.

With the parameters for the forest inventory established, the field data were appropriately recorded. Regardless of whether they were classified as common or reference trees, the DBH height of all trees was measured with a 500 mm Haglöf Sweden Mantax Blue caliper [63]. The total height of the reference trees was measured exclusively using a Haglöf Sweden Vertéx V hypsometer [64]. Figure 4.5 illustrates both measurement processes.

Figure 4.5: Diameter at breast height and total height measurement procedures.

The primary methodology for estimating the age of a tree is to analyse its growth rings [91]. It is generally assumed that each ring corresponds to one year of the tree's life.

To avoid any damage that could potentially compromise the tree's health, the Pressler increment borer is employed to take samples of the rings [92]. Thus, a sample of rings was taken from the largest tree in each study plot using a $200mm$ length, and $5.15mm$ diameter Mattson increment borer, as shown in Figure 4.6.

Figure 4.6: Growth rings sample extraction procedure.

Table 4.1 shows the main information relevant to this study, manually measured in its corresponding interest spot. Each one of the nine plots of interest was identified by the symbol "S", preceding a number. Each plot number was defined according to the field survey sequence.

Table 4.1: Summarized forest survey data in São Joanico applying the Draudt method.

Plot	**N° trees**	**Age** $[year]$	**DBH** $[cm]$		**Total height** $[m]$	
			Average	**SD**	**Average**	**SD**
S1	17	34	23.8	4.7	13.96	1.72
S2	11	34	27.5	7.1	14.89	3.68
S3	34	30	17.0	5.0	11.87	1.74
S4	16	34	22.6	4.5	15.14	2.13
S5	33	30	19.2	3.9	13.38	2.24
S6	13	34	24.4	6.2	16.21	1.39
S7	17	34	26.5	7.2	17.40	2.07
S8	18	34	25.0	5.9	18.19	3.21
S9	16	34	26.6	3.0	18.04	0.81

For the common trees, total height was derived using hypsometric equations [90].

The hypsometric coefficients are more solidly established by analyzing a single species representing a homogeneous vegetation. Equation (4.1) delineates the diameter-height relationship employed.

$$h = \frac{d}{\beta_0 + \beta_1 d}, \tag{4.1}$$

where h is the total height, given in meters (m), d the DBH, β_0 the coefficient of 1.0643, and β_1 of 0.0222 for *Pinus pinaster* [79]. Therefore, the DBH and total height of each tree in the designated regions were recorded. This scenario achieves the measurement of volume and biomass for each tree based on specific allometric equations.

Each tree had an estimated value for volume based on a specific allometric equation [90]. The result was taken considering the bark and trunk of each individual. Equation (4.2) delineates the volume equation adopted. The allometric coefficients were adopted from [93].

$$V = \beta_0 \left(\frac{d}{100}\right)^{\beta_1} h^{\beta_2}, \tag{4.2}$$

where V is the tree aerial volume (above ground), given in cubic meters (m^3), β_0 is the coefficient of 0.7520, β_1 of 2.0706, and β_2 of 0.8031 for *Pinus pinaster*.

For example, biomass is also derived from a specific allometric equation in volume estimation. Considering that, we have the following equations for biomass estimation of *Pinus pinaster* separated by tree segments.

- **Trunk**

$$w_s = \beta_0 d^{\beta_1} h^{\beta_2}, \tag{4.3}$$

  where w_s is the trunk amount biomass, β_0 is the coefficient of 0.0146, β_1 of 1.94687, and β_2 of 1.106577.

- **Branches**

$$w_{br} = \beta_0 d^{\beta_1} \left(\frac{h}{d}\right)^{\beta_2}, \tag{4.4}$$

where w_{br} is the branches amount biomass, β_0 is the coefficient of 0.00308, β_1 of 2.75761, and β_2 of -0.39381.

- **Leafs**

$$w_l = \beta_0 d^{\beta_1} \left(\frac{h}{d}\right)^{\beta_2}, \tag{4.5}$$

where w_l is the leafs amount biomass, β_0 is the coefficient of 0.09980, β_1 of 1.39252, and β_2 of -0.71962.

- **Roots**

$$w_r = \beta_0 d^{\beta_1}, \tag{4.6}$$

where w_s is the roots amount biomass, β_0 is the coefficient of 0.4522, and β_1 of 1.1294.

It is important to note that the portion displayed in Equation (4.6) is to be disregarded when attempting to estimate above-ground biomass exclusively. However, Equation (4.7) represents the appropriate portions to be effectively considered, which were previously presented in Equations (4.3), (4.4), and (4.5).

$$AGB = w_s + w_{br} + w_l, \tag{4.7}$$

where AGB is the Above Ground Biomass amount, given in kilograms (kg).

It is possible to calculate the density of a tree by considering only the above-ground portion and the corresponding volume and biomass values. It is important to note that, despite being based on the same physical principle, calculating the density of a tree does not refer to the same variable obtained when calculating the density of its wood.

When calculating the density of a tree, the mass and volume of all the different materials that make up the tree are considered. In contrast, when calculating the density of wood, only the mass and volume of one substance is considered, in this case, the wood itself. However, for this study, only the density analysis of the tree was considered, calculated as shown in Equation (4.8).

$$\rho_b = \frac{w_a}{V}, \tag{4.8}$$

where ρ_b is the tree aerial mass to volume density, given in kilograms per cubic meter (kg/m^3).

The conventional estimate of a tree's carbon is 50% of its total biomass [94]–[96]. Consequently, the carbon stock is calculated according to the portion of the tree being analysed. In this case, the focus is specifically on Above Ground Carbon (AGC), as illustrated by Equation (4.9).

$$AGC = \frac{AGB}{2}, \tag{4.9}$$

where AGC is the tree Above Ground Carbon stock, given in kilograms (kg).

To complement the forest inventory (Table 4.1), the other field data were obtained by applying allometric equations. This step was only possible after the total heights of non-dominant or sample trees had also been obtained using Equation (4.1). However, Table 4.2 provides more general information about the study sites.

Table 4.2: Biometric values obtained applying allometric equations.

Plot	**V** $[m^3]$	**AGB** $[kg]$	**AGC** $[kg]$	AGC_{ha} $[t.ha^{-1}]$	**Average** $[t.ha^{-1}]$	**SD** $[t.ha^{-1}]$
S1	6.029	3406.149	1703.074	68.12		
S2	5.858	3309.714	1654.857	66.19		
S3	5.768	3258.691	1629.345	65.17		
S4	5.267	2976.052	1488.026	59.52		
S5	7.236	4088.595	2044.298	81.77	75.18	14.57
S6	5.234	2957.396	1478.698	59.15		
S7	8.638	4880.419	2440.209	97.61		
S8	8.084	4567.271	2283.635	91.34		
S9	7.762	4385.794	2192.897	87.72		

4.2.2 LiDAR data

The scans were done by digitizing the region using point clouds generated from the Zenmuse L1 LiDAR readings. Carried by the Matrice 300 RTK UAV, this set made up the UAV-based LiDAR configuration adopted throughout the study.

Seven different scans per UAV-based LiDAR were considered, ensuring that point clouds also represented all nine plots analyzed in the field. All scans were conducted above the tree canopy, following a predetermined flight plan generated by the DJI Pilot v2.5.1.10 software. The definition of the flight parameters is shown in Table 4.3.

Table 4.3: Flight and scanning parameters configured on DJI Pilot.

Mapping	
LiDAR Mapping	Zenmuse L1
Point Cloud Density	965 $points.m^{-2}$
GSD	2.18 $cm.pixel^{-1}$
IMU Calibration	ON
Terrain Follow	ON
Terrain Follow Height	$80m$
Takeoff Speed	10 $m.s^{-1}$
Speed	5 $m.s^{-1}$
Course Angle	$0°$
Elevation Optimization	OFF
Advanced Settings	
Side Overlap (LiDAR)	80%
Side Overlap (Visible)	70%
Margin	0 m
Photo Mode	Distance Interval Shot
Payload Settings	
Return Mode	Triple
Sampling Rate	160 kHz
Scanning Mode	Repetitive
RGB Coloring	ON

Once the scans were complete, the raw LiDAR data was processed by the DJI Terra v4.0.10 software. The data was converted into ".las" format files, and their representations were configured using point clouds. The settings employed in the DJI Terra software to convert the LiDAR data are outlined in Table 4.4.

Table 4.4: Output parameters for converting LiDAR scan data to ".las" on DJI Terra.

Point Cloud Output Parameters	
Ground Point Classification	Yes
Ground Point Classification Parameters	Gentle Slope | 20 m | 6° | 0.5 m
DEM	Yes
DEM Parameters	By GSD | 0.1 m
Contour	No
Point Cloud Format	PNTS | LAS
Merged Output	Yes
LiDAR Point Cloud Block Count	3
Output Coordinate System	ETRS89 / Portugal TM06 | Default

The Zenmuse L1 LiDAR enabled the acquisition of diverse information pertinent to the study. In addition to the georeferencing of each pixel represented by the point cloud, its elevation and RGB values were also obtained. The discernibility of these characteristics is further accentuated when observing a point cloud, as illustrated in Figure 4.7.

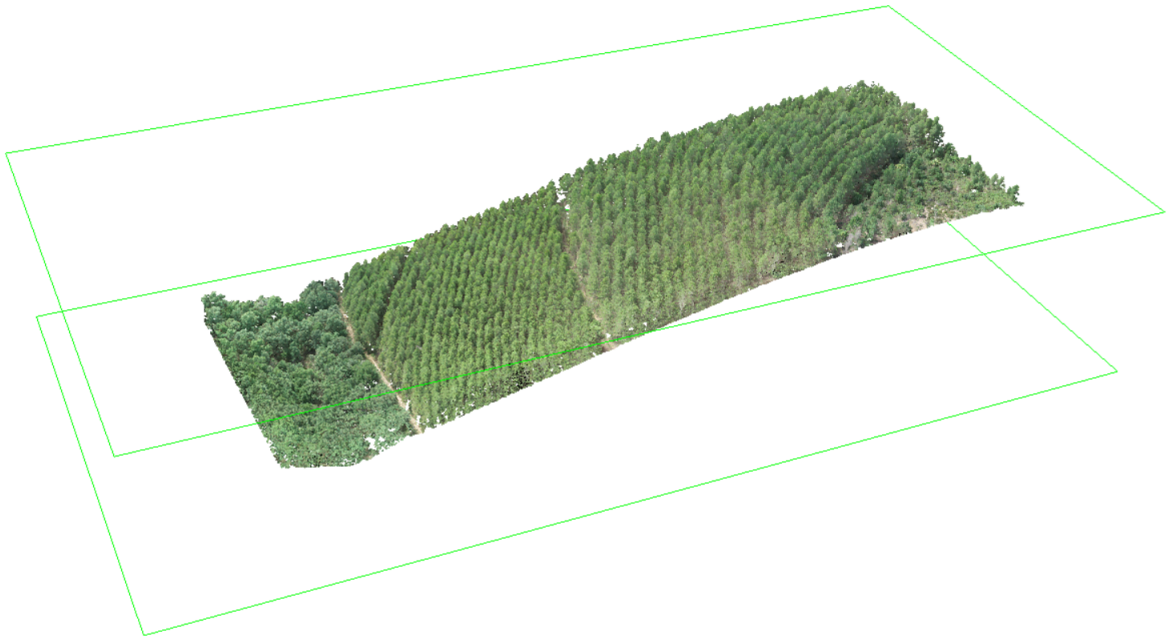

Figure 4.7: Generic point cloud from the study site in São Joanico.

4.3 LiDAR Data Processing

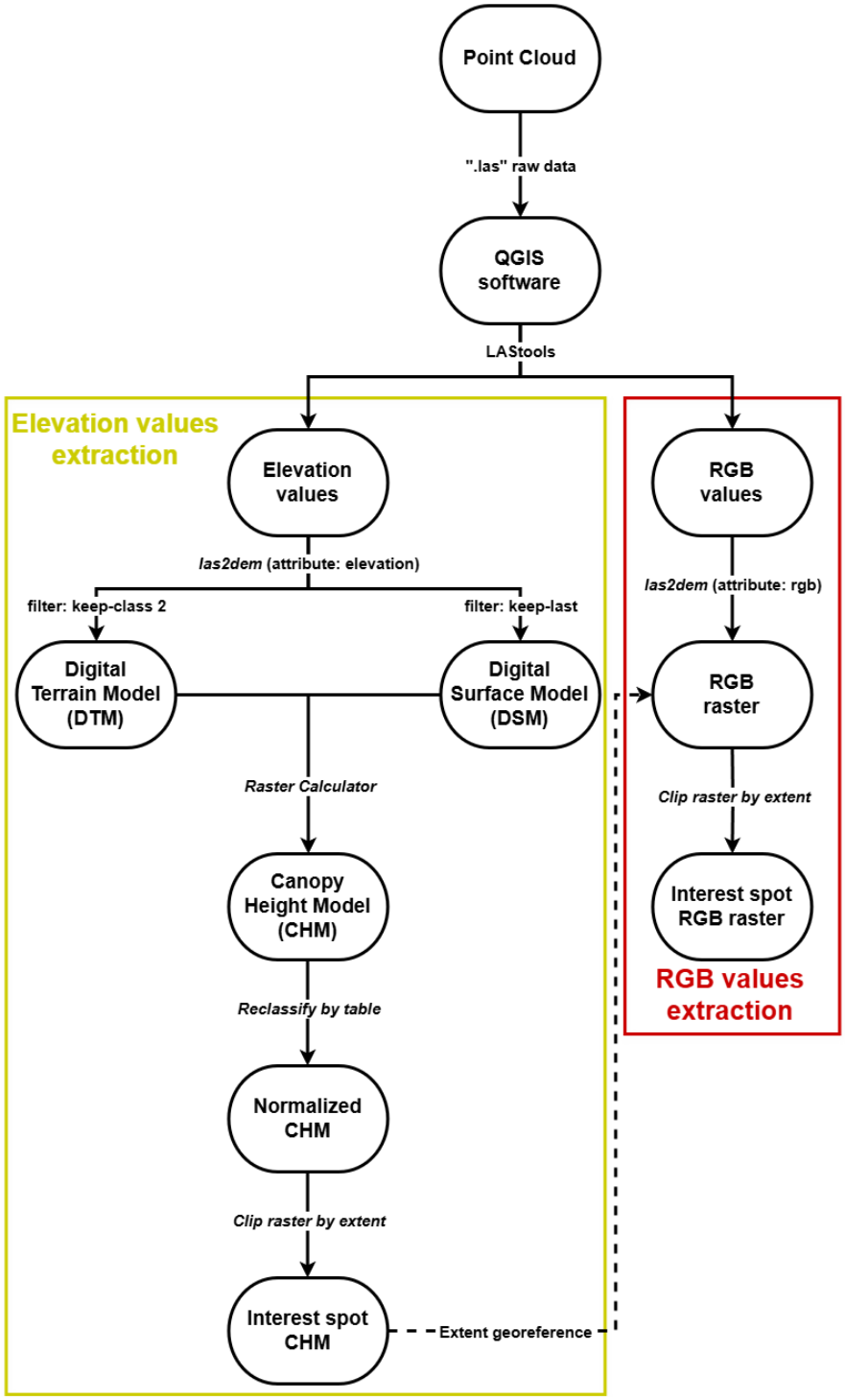

Figure 4.8: LiDAR data processing schematic.

Figure 4.8 presents an illustrative schematic of the procedures carried out during the LiDAR data processing stage. For reference of more specific contents: Figure 4.10 shows an example of obtained "Digital Terrain Model (DTM)" and "Digital Surface Model (DSM)" rasters; "Normalized CHM" is next presented in Figure 4.11; "Interest spot CHM" and "Interest spot RGB raster" are respectively presented in Figures 4.12 and 4.14.

After pre-processing the scans, the ".las" files containing their respective point cloud representations were exported to the QGIS v3.34.11 software. With the assistance of the LAStools extension, the relevant information was appropriately extracted from the point clouds.

Initially, the three-dimensional information in each ".las" file was resized to represent rasters, thus enabling a more pragmatic analysis of the information directed at each point recorded by the LiDAR. To ensure compatibility of the rasters, their dimensions were established, with each raster obtained with a resolution of 192×192 pixels, with each pixel corresponding to a real spacing of 0.1x0.1 m per pixel. This approach aligns with the study boundaries in situ, ensuring that each raster generated corresponds to an area of approximately $370m^2$, as depicted in Equation (4.10):

$$A_{raster} = (192 \times 0.1)^2 = (19.2)^2 = 368.64 \cong 370\ m^2, \tag{4.10}$$

where A_{raster} is the adopted raster dimension in absolute area scale.

Each raster's area of $370m^2$ was defined to ensure it fully covers its respective forest inventory region. Additionally, using a square delimitation facilitates the digital analysis of these boundaries in the QGIS software. As illustrated in Figure 4.9, the $370m^2$ raster delineates the $250m^2$ boundary (field data), and its geometry is also depicted.

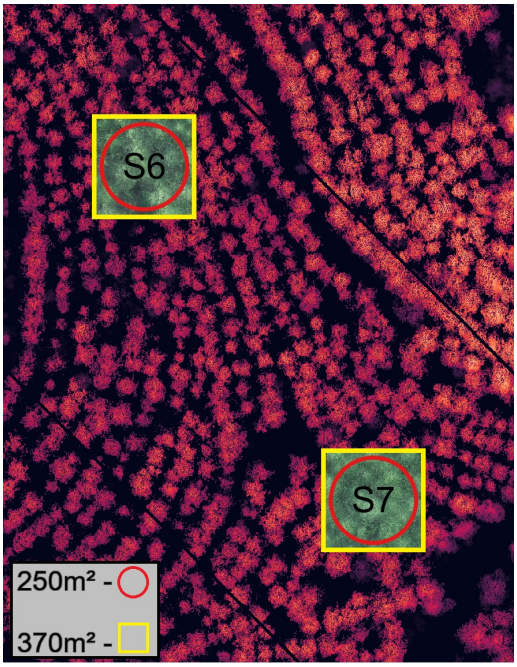

Figure 4.9: Area comparison between field and rasters study boundaries.

It is worth noting that the rasters that best represented it spatially were selected for each study boundary, ensuring that their edges were fully covered and avoiding loss of information. In addition, regions containing noise due to triangulation were analyzed to avoid basing the plot analysis on compromised areas of a given raster. Based on these considerations, each point cloud associated with a raster (R) was directed to a specific study boundary (S) and the others were ignored, as shown in Table 4.5.

Table 4.5: Interest spots linked to rasters.

Plot	**Raster**	**Raster coordinates**	
		Latitude	**Longitude**
S1 ; S2	R1	$41°09'40.4''$ - $41°09'54.1''N$	$7°47'27.6''$ - $7°47'25.7''W$
S3	R2	$41°36'28.1''$ - $41°36'16.9''N$	$6°27'54.1''$ - $6°27'49.1''W$
S4	R3	$41°36'40.1''$ - $41°36'24.8''N$	$6°27'45.3''$ - $6°27'33.9''W$
S5	R4	$41°36'27.2''$ - $41°36'16.1''N$	$6°27'41.7''$ - $6°27'36.3''W$
S6 ; S7	R5	$41°36'34.5''$ - $41°36'17.9''N$	$6°27'36.0''$ - $6°27'26.7''W$
S8	R6	$41°36'32.8''$ - $41°36'16.0''N$	$6°27'27.5''$ - $6°27'21.8''W$
S9	R7	$41°36'30.9''$ - $41°36'14.7''N$	$6°27'23.9''$ - $6°27'19.3''W$

All files generated for the rasters were saved in Tagged Image File Format (TIFF)

format. This definition was adopted because the TIFF format is ideal for storing values related to different attribute categories, such as elevation or RGB values.

4.3.1 Elevation Values Extraction

To access the effective elevation values, considering the height of the trees, it was necessary to generate different DEMs. Using the LAStools "las2dem" tool, the DTM and DSM of each point cloud were generated. The procedures differ only in selecting the desired filter, which directly implies the elements to be represented in each DEM.

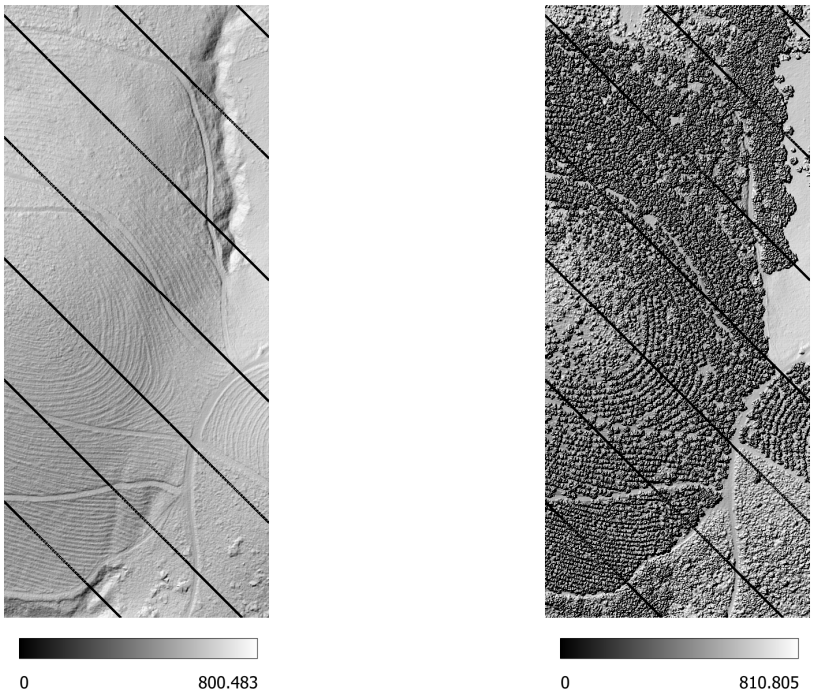

(a) DTM (b) DSM

Figure 4.10: Generated DTM and DSM of the same study plot.

The DTMs were the first DEMs to be extracted from the point clouds. The "keep-class 2" filter was applied to extract only soil-related elements, assigning them to the output raster. Subsequently, the "keep-last" filter was employed to generate DSMs, incorporating the representation of trees into the output raster. The "elevation" attribute was assigned

to extract both rasters, thereby labeling each pixel with a georeferenced altitude value. The rasterized DTM and DSM of the same point cloud are shown in Figure 4.10.

The "Raster Calculator" option in QGIS was employed to subtract the already reclassified DTM and DSM rasters. The operation was executed by subtracting from each DSM pixel the respective local ground elevation values represented by the DTM. Consequently, each point cloud's rasterized CHM was generated. In forestry, each pixel value of the CHMs denotes the vertical distance, that is, the height of the trees in a specific location. Figure 4.11 shows the CHM raster generated from the same region illustrated in Figure 4.10.

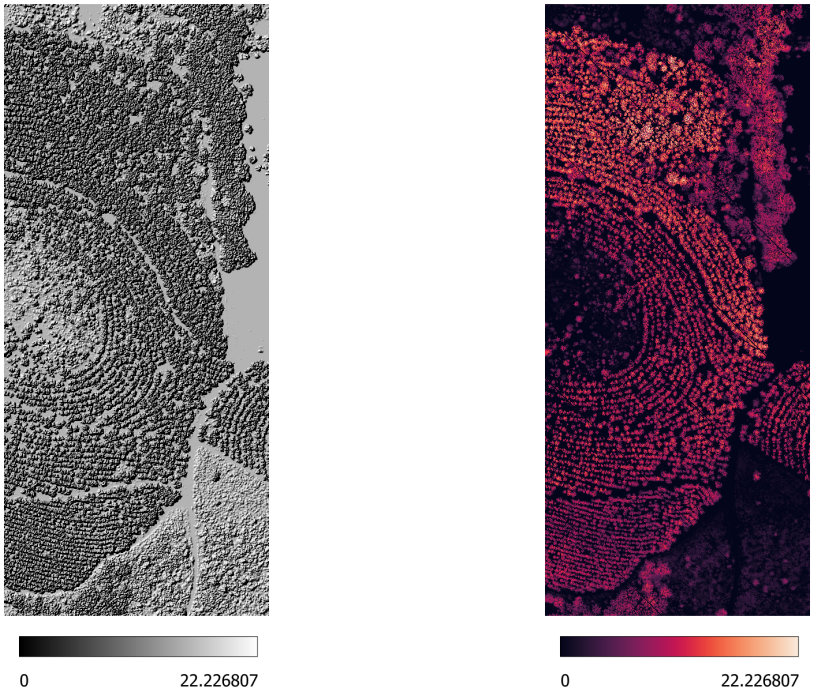

(a) CHM - Hillshade (b) CHM - Singleband pseudocolor

Figure 4.11: Generated CHMs of the same study plot.

However, it should be noted that small natural depressions, as well as multiple reflections caused by dense foliage, can result in erroneous interpolation of LiDAR scans [97]–[99]. These flaws can cause noise, generating negative values and a CHM. To overcome this irregularity, the QGIS "Reclassify by table" tool was applied, reclassifying the

negative values to zero and avoiding possible contamination in future results.

To enhance the visibility of the variations in tree heights within the CHMs, the rendering model of each raster was modified from the default "Hillshade" setting to "Singleband pseudocolor". This adjustment enabled the precise observation of disparities in points about the vegetation and ground altitude. This methodological approach facilitates the visual examination of a specific region, as illustrated in Figure 4.11.

Subsequently, employing the geographic references delineated in the field by the LT800 GPS, each study boundary was meticulously extracted from its respective CHM. The "Clip raster by extent" tool, already available in QGIS by default, was used to separate the boundaries of interest from its CHM, respecting its delimitation. The resultant rasters, as depicted in Figure 4.12, illustrate the successful extraction process:

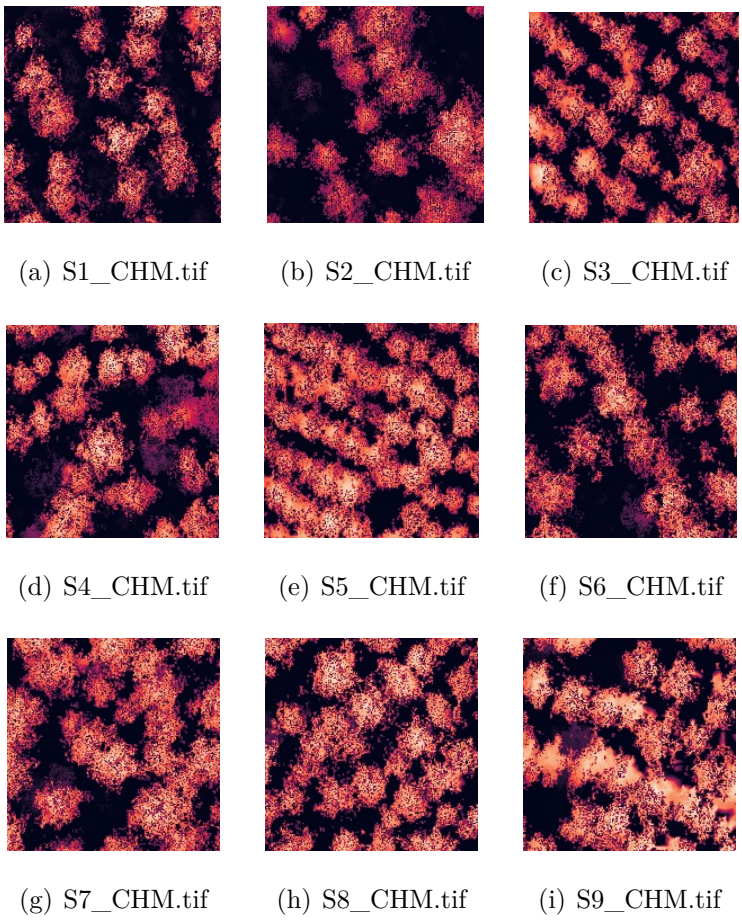

(a) S1_CHM.tif (b) S2_CHM.tif (c) S3_CHM.tif

(d) S4_CHM.tif (e) S5_CHM.tif (f) S6_CHM.tif

(g) S7_CHM.tif (h) S8_CHM.tif (i) S9_CHM.tif

Figure 4.12: Interest regions of study CHM clipped rasters.

4.3.2 RGB Values Extraction

The extraction of RGB values was carried out by the steps developed during the extraction of elevation values described in 4.3.1. Once again, the "las2dem (file)" tool was applied, but the extraction attribute for each point cloud was set to RGB. The filter option was not configured, requiring the values relating to the region's coverage to be displayed directly. In contrast to the single return layer characteristic of elevation rasters, the rasters generated for RGB values exhibited three distinct layers, each corresponding to a different color band.

Presented in Chapter 2, many studies employ satellite RGB images considering vegetation covered areas monitoring [18], [23], [24]. This framework contains advantages, such as open access and continental extensions available. Furthermore, larger resolutions are typical of satellite data acquisitions. 10x10m resolution of Sentinel-2 is one of the refinements in satellite data acquisition.

Less explored in the academic scenario, some countries conduct imagery scans of their territories. The RGB images by standard are obtained by conventional cameras with advanced configurations during airplane overflights. Being closer than satellites, the obtained orthophotomaps tend to present a better resolution. Also, it provides free access to a large amount of data.

Figure 4.13 presents a comprehensive comparison between RGB displays by orthophotomap and satellite of a generic plot obtained from the study site. Figure 4.13(a), presents an effective LiDAR acquisition obtained during this work. Meanwhile, Figure 4.13(b) shows a 0.25x0.25 m resolution orthophotomap of Portugal scanning carried out in August 2021, available in [100]. Finally, a Sentinel-2 RGB return imagery with 10x10 m resolution in the same region was obtained from [101], as illustrated in Figure 4.13(c).

(a) Zenmuse L1 scan (0.1x0.1m)

(b) Continental Portugal orthophoto (0.25x0.25m)

(c) Sentinel-2 satellite imagery (10x10m)

Figure 4.13: Different RGB displays within the same coordinates on QGIS.

The orthophoto is more similar to the UAV-based LiDAR imagery acquisition than satellites. Even considering a refined resolution for satellite acquisition, minimal details can be recognized comparing Sentinel-2 imagery with LiDAR and orthophotography. This type of image acquisition is not as continuous as satellite imagery, but it does not cover such a long period of time (more than five years) as to have a significant impact on variables such as land use.

Finally, each study boundary was meticulously extracted from its corresponding RGB raster. To achieve this, the CHM rasters previously generated for each plot served as a reference, incorporating field georeferencing (Figure 4.12). Consequently, an RGB raster was obtained for each boundary, respecting its delimitation, resulting in a profile analogous to that of conventional RGB images, as depicted in Figure 4.14.

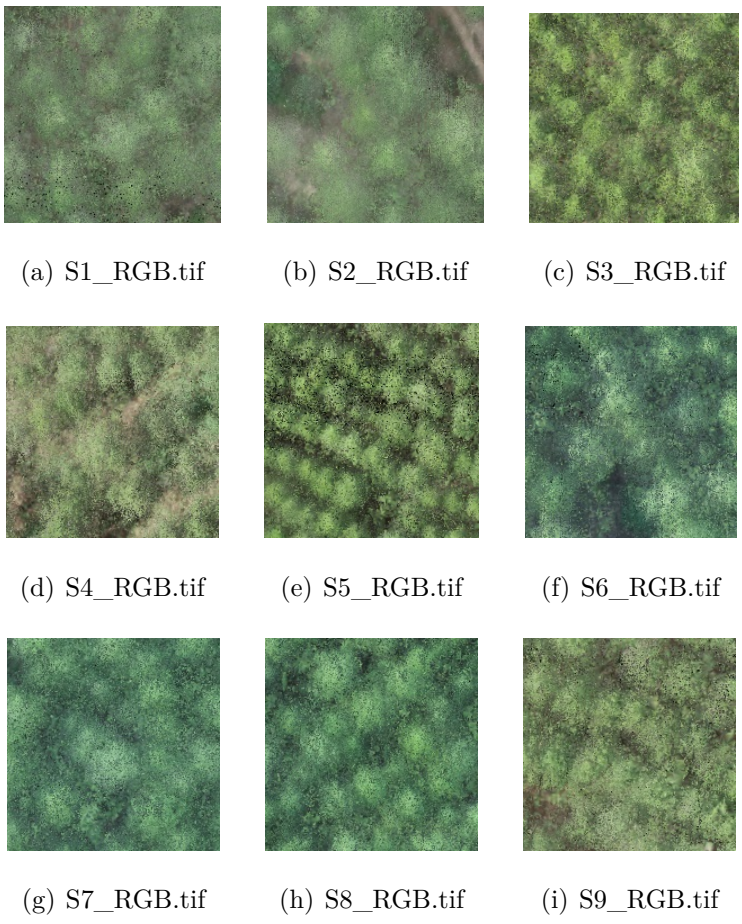

(a) S1_RGB.tif (b) S2_RGB.tif (c) S3_RGB.tif

(d) S4_RGB.tif (e) S5_RGB.tif (f) S6_RGB.tif

(g) S7_RGB.tif (h) S8_RGB.tif (i) S9_RGB.tif

Figure 4.14: Interest plots of study RGB clipped rasters (São Joanico).

4.4 Dataset

To increase the quantity of data, the initial nine CHM and RGB rasters were divided into nine complementary parts, according to a fixed pixel resolution. This approach is a common one in Deep Learning and similar applications, and is essential for improving the accuracy obtained by the algorithm during the training and validation stages [102].

With the standardized resolution of 192×192 pixels for each raster, as outlined in Section 4.3, the divisions were made respecting the delimitation of 64×64 pixels. This specific choice was previously analysed in the study [83]. Consequently, nine distinct data samples were extracted from each raster to analyze heights and images, providing 81 potential labels for analysis.

The following section delineates the methodology for manipulating the information contained in each sample, including the height and RGB values. Each of the 81 samples was assigned a label called "*filename*" to identify its related values uniquely. This identification was applied using the numbering of its predecessor raster, followed by the index of the row and column corresponding to extracting its information through the application of the 64×64 pixel mask. This definition will be shown later in Figure 4.16, clarifying how it was applied in practice.

Standardizing the samples ensured a resolution of 64×64 pixels, considering the real spacing of $0.1 \times 0.1m$ for each pixel. Therefore, each sample has a real area of approximately $41m^2$, as described in Equation 4.11:

$$A_{64x64} = (64 \times 0.1)^2 = (6.4)^2 = 40.96 \approx 41\ m^2, \tag{4.11}$$

where A_{64x64} is the adopted sample dimension in absolute area scale.

4.4.1 Height Extraction

The Python language was used to extract the height values from each CHM raster, with the resolution of 64×64 pixels per sample being respected. The mean of the pixel

values was subsequently calculated, associating a single height value with each sample.

However, it was observed that some samples contained substantial volumes of low values, which were attributed to the presence of soil or undergrowth. This range of values, present in all the samples, albeit in different proportions, generated slight interferences in the analyzed results. When calculating the average, incorporating these soil values slightly reduces the final value assigned to each sample.

To mitigate this interference, a filter was implemented to ascertain which elevation values would be considered when calculating the mean. The filter threshold was set at 1.3 m to exclude soil values and those associated with undergrowth or shrubs, undesirable elements for this study.

This reference height is a widely accepted technique in forestry analysis, frequently employed to exclude contributions from elements below 1.3 m. This same value is adopted as a reference for measuring DBH, an essential metric in forest inventories [2].

As illustrated in Table 4.6, applying the "*above 1.3 filter*" results in height averages exhibiting enhanced integrity. The pertinence of this data treatment had previously been underscored by the study [83].

Table 4.6: *above 1.3 filter* influence in average height values at spot $S2$.

Filename	**No filtering**		***Above 1.3 filter***	
	Average_height $[m]$	**SD** $[m]$	**Average_height** $[m]$	**SD** $[m]$
two_0_0.png	2.69		6.17	
two_0_1.png	6.18		7.38	
two_0_2.png	0.78		5.17	
two_1_0.png	1.19		5.26	
two_1_1.png	3.20	1.73	6.64	0.85
two_1_2.png	4.69		7.63	
two_2_0.png	2.20		6.19	
two_2_1.png	2.84		6.64	
two_2_2.png	4.49		6.8	

Despite implementing the *above 1.3 filter*, a notable difference existed between the real and calculated values from the CHM rasters. The highest values of each pixel related to each tree were recorded, considering the intermediate height of its branches and leaves.

This discrepancy requires normalization of the height averages in each sample. To enhance the reliability of the findings, this study examined the total heights directly extracted in the field. Consequently, each boundary's global average height was compared with its standard plot's total height. This approach observed an approximate relationship between the values, as illustrated in Table 4.7.

Table 4.7: Ground truth total heights and filtered heights of rasterized plots comparison.

Plot	**Total height (field data)** $[m]$	**Filtered height (QGIS raster)** $[m]$	**Field-raster ratio** $[m]$	**SD** $[m]$	**Average ratio** $[m]$
S1	13.93	6.17	2.26		
S2	12.90	6.44	2.00		
S3	15.45	6.37	2.43		
S4	14.78	6.90	2.14		
S5	15.10	7.20	2.10	0.23	2.06
S6	16.30	7.55	2.16		
S7	16.47	8.25	2.00		
S8	17.07	9.23	1.85		
S9	15.44	9.47	1.63		

Given the relatively modest SD of 0.23 m, the value of the global field raster rate does not vary significantly from one boundary to another. Consequently, adopting the mean of the international rates as a metric for normalizing the average heights of the rasters to total heights appears to be a partially reliable approach. As delineated in Section 3.1.5, total height is designated as the search variable in this study, underscoring the need to acquire it accurately.

To facilitate generalization, Figure 4.15 shows the behavior of the field raster rates for

each of the 81 samples, adopting the global ratio of 2.06 m as a reference, as well as its upper and lower limits, considering the SD of 0.23 m.

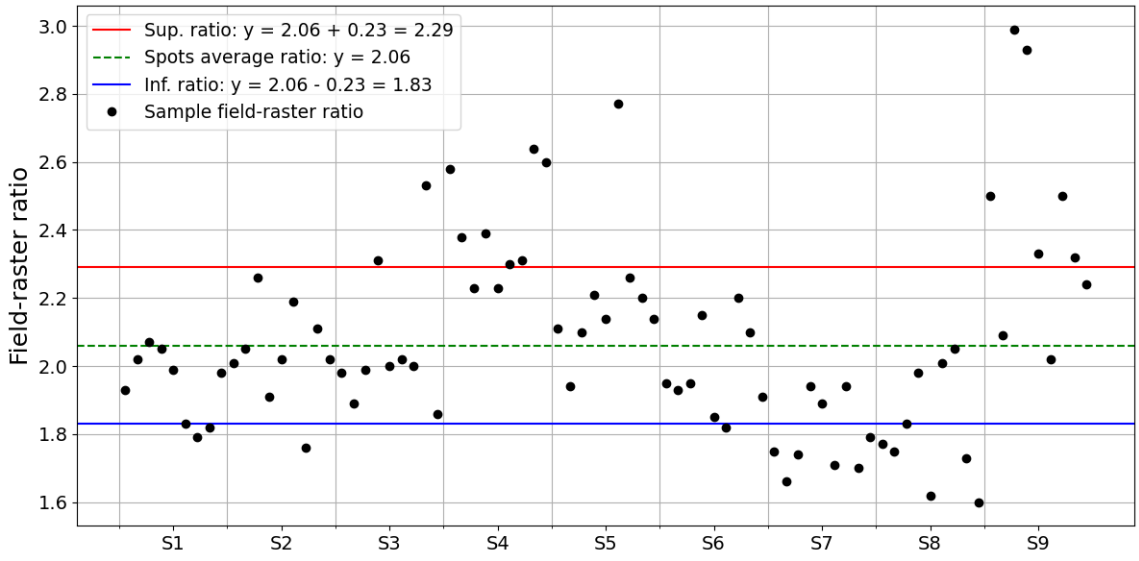

Figure 4.15: Sample field-raster comparison adopting 2.06 as normalization parameter.

4.4.2 Coverage Extraction

Despite the *above 1.3 filter* implementation, each 64×64 sample had specific pixels ignored according to their indexed values. This strategy resulted in splitting the values to be validated and the values to be ignored during the averaging process. Consequently, the percentage of values to be considered in calculating the mean height was extracted from each sample.

Furthermore, the validation percentages were normalized, with their values distributed between zero and one. The highest and lowest percentages among the analyzed samples were identified to accomplish this. Consequently, a maximum value of one (1.0) was assigned to the highest rate, and zero (0) was assigned to the lowest. The percentage values assigned to each sample before and after normalization are presented in Table 4.8. Only percentages related to the spot $S2$ were presented, including the lower value of 0.132, normalized to 0.

Table 4.8: 0 to 1 normalization on validation percentages at spot $S2$.

Filename	**Original**		**Normalized**	
	Validation percent	**SD**	**Validation percent**	**SD**
two_0_0.png	0.423		0.415	
two_0_1.png	0.828		0.992	
two_0_2.png	0.132		0	
two_1_0.png	0.195		0.090	
two_1_1.png	0.471	0.219	0.484	0.312
two_1_2.png	0.604		0.673	
two_2_0.png	0.341		0.298	
two_2_1.png	0.415		0.403	
two_2_2.png	0.642		0.727	

The calculation of average height values, while providing appropriate measurements, does not consider the number of trees in each sample. This is because a single value is assigned irrespective of forest density. However, this distinction between samples is essential for the final analysis of carbon sequestration.

Determining percentages related to values greater than $1.3m$ suggests the ideal scenario for analyzing vegetation cover in each sample. This strategy circumvents the potential inconsistency of not considering local forest stand density.

The broad distribution of the *pinus pinaster* species contributes to diverse analyses of its stand density. The diversity of environmental conditions in which it can be found generates instability in the relationship between age and total height of the species [103].

In [104] an average of 913 trees per hectare was proposed, following a comprehensive analysis of 274 forest inventories of *pinus pinaster* across diverse regions of Portugal. This analysis was conducted for forestry-intended colonies, encompassing a variety of ages of the species [104]. The study [105] covered five regions of Portugal, founding stand densities of 844, 512, and 574 trees per hectare for ages 33, 34, and 36 years, respectively. Furthermore, [106] contended that for the age range of 30 to 35 years, the species exhibits

an average density of 700 trees per hectare, as evidenced by the study conducted in proximity to Lisbon, Portugal.

Therefore, using stand density values directly from the study plot is more appropriate. During the forest inventory, the number of trees analyzed in each $250m^2$ boundary was recorded, as shown in Table 4.9. Additionally, the study site comprises colonies with trees 30 and 34 years old, based on the interest boundaries growth rings analyses (4.2.1).

Table 4.9: Colonies age stand densities obtained by forest inventory in São Joanico.

Plot	**Age** $[year]$	**250**m^2			**Hectare**		
		N_{250m^2}	**Average**	**SD**	$N_{hectare}$	**Average**	**SD**
S1	34	17			680		
S2	34	11			440		
S3	30	34			1360		
S4	34	16			640		
S5	30	33	≈ 19	≈ 8	1320	≈ 778	≈ 331
S6	34	13			520		
S7	34	17			680		
S8	34	18			720		
S9	34	16			640		

The elevated stand density values associated with plots $S3$ and $S5$ contribute to the sudden increase in the average and the relatively high SD value. In addition to their reduced occurrence in the study area, younger stands, such as 30-year-old stands, correspond to a minority of the boundaries. To avoid contamination of the metrics, Table 4.10 shows the data evaluation excluding the youngest plots.

Table 4.10: Most representative stand densities of colonies in São Joanico.

Plot	**Age** $[year]$	**250**m^2			**Hectare**		
		N_{250m^2}	**Average**	**SD**	$N_{hectare}$	**Average**	**SD**
S1	34	17			680		
S2	34	11			440		
S4	34	16			640		
S6	34	13	≈ 15	≈ 3	520	≈ 617	≈ 100
S7	34	17			680		
S8	34	18			720		
S9	34	16			640		

Furthermore, the study site exhibits an average density of 15 trees per $250m^2$, or 617 trees per hectare. In this way, the correction shown in Equation 4.12 was established to obtain a reliable number of trees contained in the $370m^2$ regions of the rasters:

$$N_{370m^2} = \frac{N_{250m^2} \times A_{raster}}{A_{forest-inventory}} = \frac{N_{250m^2} \times 370}{250}, \tag{4.12}$$

where N_{370m^2} is the corrected number of trees per $370m^2$, N_{250m^2} is the number of trees related to each forest inventory, as previously shown in Tables 4.9 and 4.10, and $A_{forest-inventory}$ is the standard area established for each forest inventory.

Table 4.11 shows the number of trees assigned to each raster after correction, applying Equation 4.12:

Table 4.11: Stand density values for each 34-year age colonies for raster extension.

Plot	N_{370m^2}	**Average**	**SD**
S1	25		
S2	16		
S4	24		
S6	19	23	4
S7	25		
S8	27		
S9	24		

As illustrated in Table 4.11, the number of corrected trees exhibits a relatively low Standard Deviation of $SD = 4$ trees. This supports using the average number of 23 trees per $370m^2$ as a parameter to relate to the validation percentage variable for each 64×64 sample.

However, as delineated in Equation 4.11, each sample constitutes an area of $41m^2$, suggesting an average of 3 trees per sample. This expectation is shown in Equation 4.13:

$$N_{SJ\_41m^2} = \frac{\overline{N_{370m^2}} \times 41}{370} \approx \frac{\overline{N_{370m^2}}}{9} = \frac{23}{9} \approx 3\ trees, \tag{4.13}$$

where, $N_{SJ\_41m^2}$ is the estimated number of trees per $41m^2$ in São Joanico, and $\overline{N_{370m^2}}$ is the average number of trees per $370m^2$ obtained in Table 4.11.

Employing the normalized validation percentages, as delineated in 4.4.2, enables allocating a specific number of trees per sample. The percentage value of forest cover is linked to the base value obtained by each sample to calculate its carbon sequestration. To achieve this objective, three intervals were designated, correlating the percentage validation to the number of trees, as illustrated in Table 4.12. The second band was assigned a wider range directly related to the value obtained in Equation 4.13.

Table 4.12: "*N° trees*" values validation intervals.

Validation interval [%]		**N° trees**
0 - 0.3	$\longrightarrow$	2
0.3 - 0.7	$\longrightarrow$	3
0.7 - 1	$\longrightarrow$	4

4.4.3 RGB Images Division

As delineated in Section 4.3.2, the top views related to the RGB raster of each of the nine plots can be used as RGB images. This feasibility is facilitated after extracting only the regions of interest, as demonstrated in Figure 4.14.

The same georeferencing delimitations for extracting 64×64 samples, as defined in Section 4.4.1, were also applied to the original RGB images, which were subsequently split. This approach enabled the association of the average height and validation percentage values to an RGB image in the same $41m^2$ area.

The original RGB representations, stored in ".tif" format, were split using code written in the Python language. The RGB images, characterized by a resolution of 64×64 pixels, were stored in the ".png" format. Although not as robust as the ".tif" format, the ".png" format can sufficiently support low-resolution images without distorting their information, as is evident in this case.

Consequently, each 192×192 pixel image provided nine different complementary RGB images of the same study plot. As outlined in 4.4, each of the 81 RGB images was uniquely identified by the "*filename*" label. The adopted tagging standard for the RGB images associated with a single raster is shown in Figure 4.16.

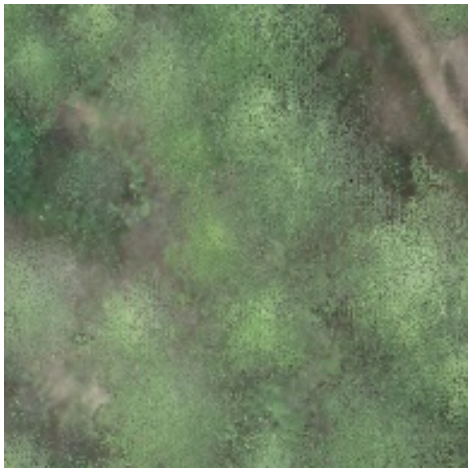

(a) S2_RGB.tif

(b) two_0_0.png

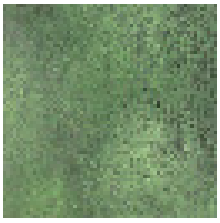

(c) two_0_1.png

(d) two_0_2.png

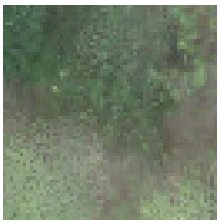

(e) two_1_0.png

(f) two_1_1.png

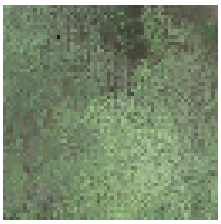

(g) two_1_2.png

(h) two_2_0.png

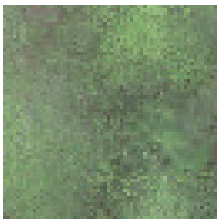

(i) two_2_1.png

(j) two_2_2.png

Figure 4.16: Splitting the 192×192 image (.tif) into nine 64×64 RGB images (.png).

4.4.4 Labels Structure

Before it was directed to the learning structures, all the numerical information was stored in a ".csv" file. Except for the first, the rows stored information related to a specific sample. The header delineated a reference pertinent to each attribute stored by the samples, which are as follows:

- ***filename***: Unique identification of the sample, obtained after generating 64×64 images. Described in Section 4.4.3;

- ***height***: Average height value of the 64×64 CHM boundaries after applying the "*above 1.3 filter*". Described in Section 4.4.1;

- ***coverage***: Normalized percentage of values considered for calculating the average height in each sample. Described in Section 4.4.2.

Thus, the values for each 64×64 sample were stored correctly. Furthermore, tagging with "*filename*", each set of values could be easily associated with its corresponding RGB image with the same label.

Figure 4.17 elucidates the procedures for obtaining the labels up to the establishment of the dataset. To provide context to the most specific content: "Average height" is the filtered average value, as shown in Table 4.6; "*height*" is the normalized labeled value for the average height by the 2.06 ratio achieved in Table 4.7 and illustrated in Figure 4.15; "Validation percentage" is the percentage of values validated after applying the "*above 1.3 filter*", as first described in Section 4.4.2; "*coverage*" is the 0 to 1 normalized "Validation percentage", as exemplified in 4.8; "RGB image" is the 64×64 pixels images in ".png" format (Figure 4.16); "*filename*" is the reference of each sample directly related to its RGB image (Figure 4.16).

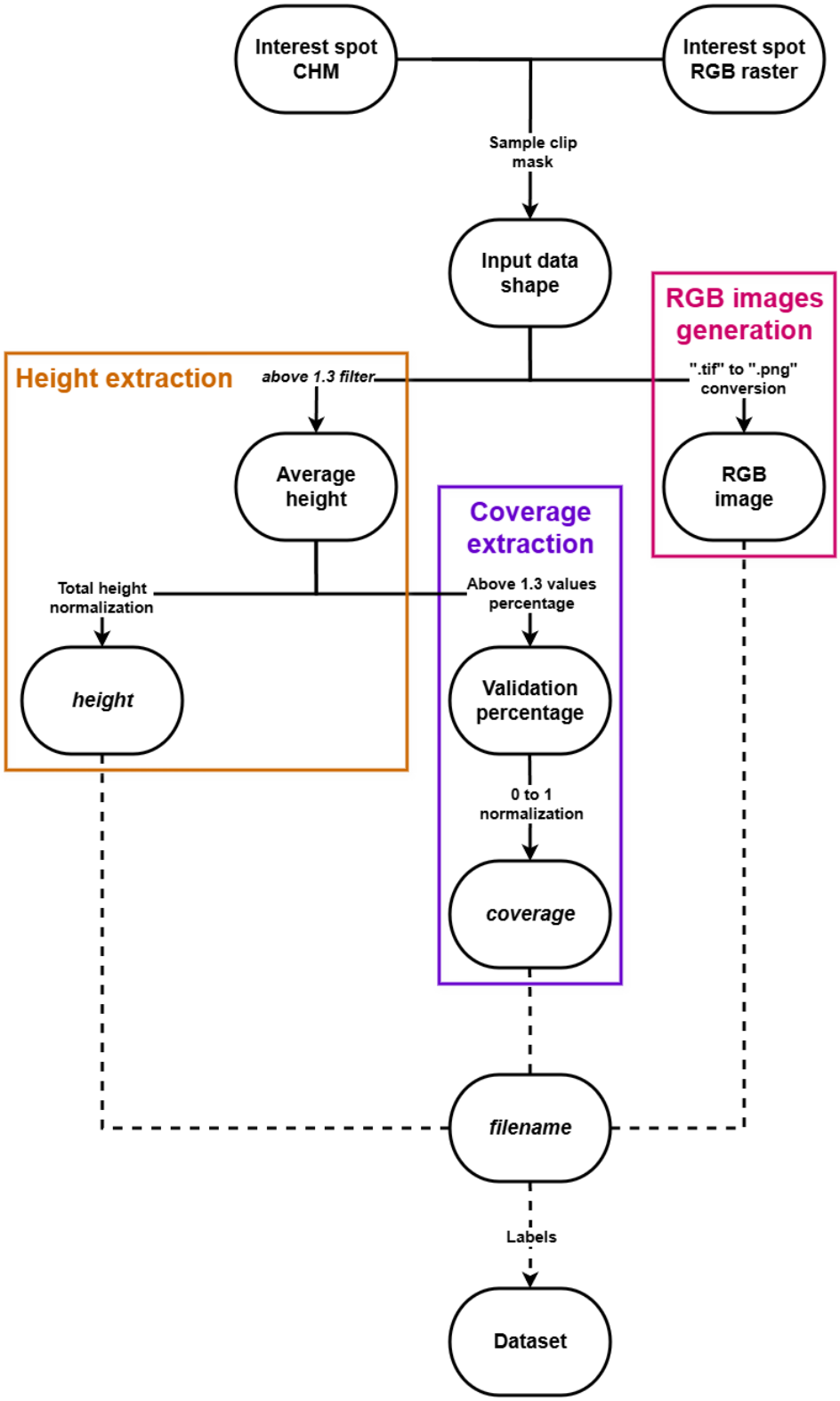

Figure 4.17: Dataset configuration schematic.

Figure 4.13 shows an overview of the dataset, summarizing the 81 total samples.

Table 4.13: Simplified dataset labels displacement.

filename	***height*** $[m]$	***coverage*** $[\%]$
one_0_0.png	11.83	0.150
one_0_1.png	12.79	0.478
one_0_2.png	13.67	0.566
one_1_1.png	13.68	0.380
one_1_2.png	13.28	0.340
⋮	⋮	⋮
nine_1_1.png	21.68	0.898
nine_1_2.png	17.54	0.755
nine_2_0.png	17.15	0.410
nine_2_1.png	20.37	0.965
nine_2_2.png	22.03	0.952

4.4.5 Dataset Split

The dataset, composed of 81 RGB images and their corresponding numerical information, was divided into training/validation and test. This split ensured that the algorithm could not access the test set during the training and adjustment of the CNN. Using the test set to assess the reliability of the CNN would thus indicate a more solid accuracy of the trained model.

In view of the relatively small amount of data, a 90/10 split between the training/validation set and the test set was chosen [107]. This division has been previously examined in the scientific literature and showed better fitting than other divisions such as 50/50, 60/40, 70/30, and 80/20 [108].

To optimize the generalization of the CNN after training, a second division of the data within the training/validation set was carried out. The k-Fold Cross Validation methodology was applied to enhance the reliability of the results [55]. Based on scientific literature, and considering the 73 images, the training/validation set was subdivided into five parts, adopting "$k = 5$" [109].

Substantial attempts for random split training/validation set into five folds were analyzed using Python code. This approach was adopted to establish folds that were more representative of the dataset as a whole. In addition to the folds, the representativeness of the test set was also delineated. The consistency inspection of each applied the average and standard deviation measurements, as shown in Table 4.14:

Table 4.14: Dataset split evaluating comparison.

Set	**N° labels**	***height*** $[m]$		***coverage*** $[\%]$	
		Average	**SD**	**Average**	**SD**
k-fold 1	15	15.51	0.22	0.657	0.045
k-fold 2	15	15.47		0.619	
k-fold 3	15	15.32		0.561	
k-fold 4	14	15.38		0.610	
k-fold 5	14	15.49		0.670	
test	8	15.95		0.693	

The comparison indicates that both sets adequately represent the amount of data, as evidenced by the SD values of 0.22 m and 4.5% for "*height*" and "*coverage*", respectively. This hypothesis is supported by the low deviations from the respective means, which suggests low dispersion, thereby providing the analyzed data with greater internal consistency.

4.5 Algorithms Implementation

Following the split and inspection of the dataset, the performance evaluation stage of the Deep Learning (DL) algorithms proceeded. Employing diverse configurations of convolutional layers for identifying patterns in images frequently results in discrepancies in accuracy among different CNN architectures. Figure 4.18 shows the procedures carried out from the CNN models implementation to the obtained outputs.

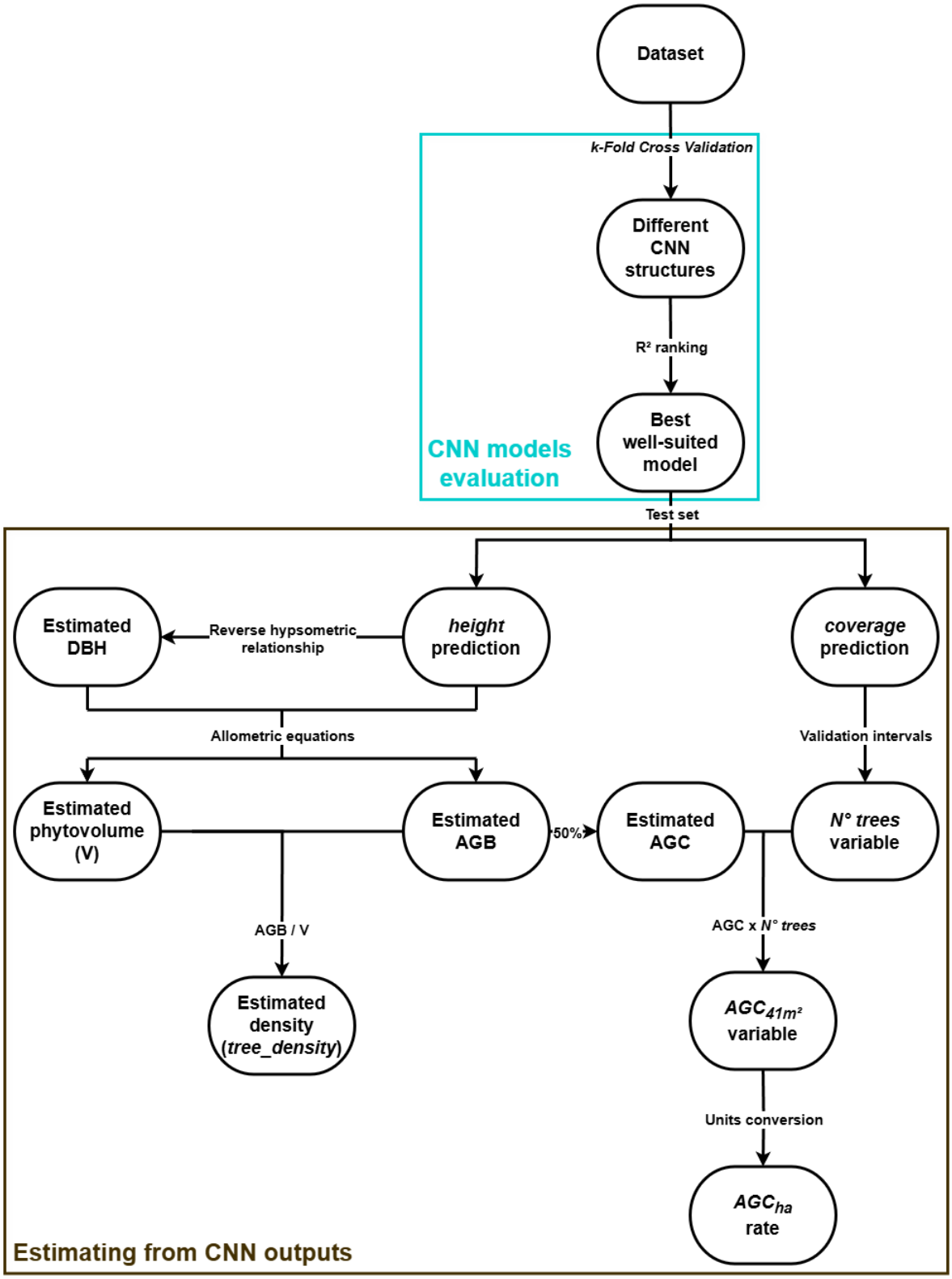

Figure 4.18: Algorithms implementation schematic.

The topics illustrated in Figure 4.18 are better described in their respective sections, as identified by the colored squares. Some context of these contents are as follows: "Best well-suited model" was the stage that defined the model with best predicted performance achieved by R^2 ranking (Section 4.5.1); "*height* prediction" and "*coverage* prediction" are the best fitted model prediction results related to their extracted values, respectively described in Sections 4.4.1 and 4.4.2; "Estimated DBH" is the achieved DBH by reverse hypsometric relationship, as presented in Equation (4.14) corresponding to the predicted total height value; "Estimated phytovolume (V)", "Estimated AGB", "Estimated density (*tree_density)*", and "Estimated AGC" were accessed respectively by Equations (4.2), (4.7), (4.8), and (4.9), based on the predicted height and estimated DBH values; "$N°$ *trees* variable" is based on the predicted *coverage* interval correspondence (Table 4.12); "AGC_{41m^2} variable" is the estimated carbon sequestration encompassed in the sample area of $41m^2$, as described in Equation (4.15); "AGC_{ha} rate" is the proportional value obtained from "AGC_{41m^2} variable", as described in Equation (4.16).

4.5.1 CNN Models Evaluation

To ensure a more neutral comparison, six distinct CNN models (outlined in Section 3.2.3) were implemented under the same conditions. The implementation of these configurations and libraries in Python is outlined as follows:

- "*input_shape*" fixed at 3 layers of 64×64 pixels for input RGB images;
- "*KFold*" function, from the "*sklearn.model_selection*" library for implementing the "k-Fold Cross Validation" methodology, setting "$k = 5$";
- "*early_stop*" in validation loss monitoring ("*val_loss*");
- "epochs" set to 100 during the model training/validation stage;
- "*batch_size*" set to 8.

As defined in [46], "patience" is the tolerance of times to register worsening values in the validation stage until stopping it. Different patience values were employed during the "*early_stop*" monitoring to avoid overfitting during the model training stage. Each architecture was trained for four distinct patience values: 7, 10, 15, and 20.

The R^2 values obtained in the test phase for each architecture were compared to select the most suitable model. This choice is based on the fact that higher R^2 values directly indicate a greater degree of learning on the part of the model. In essence, the higher the R^2 value, the more proficient the model is in interpreting the patterns of interest present in the input data.

As delineated in Section 3.2.4, the remaining evaluation metrics were calculated and monitored for each model during the training, validation, and testing stages. However, these metrics were analyzed in greater depth only for the model with the highest R^2, considering that its performance tends to be proportional to this indicator. The six split sets (Table 4.14) were subjected to the same evaluation criteria, providing a more comprehensive view of the final model performance.

4.5.2 Estimating from CNN Outputs

After establishing the best-suited model, the other variables estimated from the predicted values were obtained using only that model. Given the relatively triviality of the equations, with no need for complex manipulations and fixed constants, the subsequent variables were conveniently implemented in Python.

As demonstrated in Section 4.2.1, in addition to total height, Diameter at Breast Height (DBH) is also a crucial variable when applying allometric equations. However, a reverse hypsometric equation was formulated to estimate DBH from the total height value predicted by the algorithm.

During the field data collection process, all the DBH and total height values of the trees in the study regions were obtained as described in Section 4.2.1. All the diameters and their respective heights, whether measured from the dominant/sample trees or estimated

by Equation (4.1), were added to a single graph (Figure 4.19).

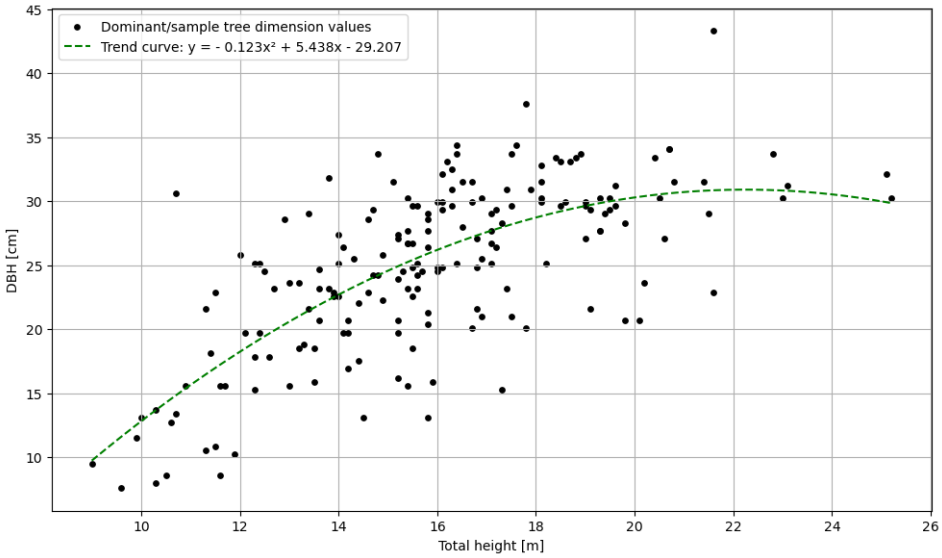

Figure 4.19: Reverse hypsometric relationship obtained by trend curve.

The final step entailed the mathematical representation of this polynomial trend curve, providing a height value for an input diameter value. Equation 4.14 presents the reverse hypsometric equation, which was developed directly from the local data:

$$DBH = -0.123\widehat{h}^2 + 5.438\widehat{h} - 29.207, \tag{4.14}$$

where DBH is the estimated Diameter at Breast Height in centimeters (cm), and $\widehat{h}$ is the predicted total height, defined by "*height*" variable.

With the VGG19 structure already trained and validated, using the average DBH and total height values, variables such as volume, biomass, density, and, finally, carbon, were also assigned to each image during the test phase. These variables were calculated by their respective equations, as defined in Section 4.2.1. These equations had previously been used during the analysis of field data.

Furthermore, the intervals delineated in Section 4.13 were implemented. Employing the normalized validation percentages predicted for each image, a specific number of trees was allocated. This approach was instrumental in providing a more reliable average of

the real proportion of carbon sequestration associated with each image. This estimate was made using Equation (4.15):

$$AGC_{41m^2} = \widehat{AGC} \times N_{41m^2}, \tag{4.15}$$

where AGC_{41m^2} is the amount AGC in kilograms (kg) contained in the sample boundaries ($41m^2$), and $\widehat{AGC}$ is the estimated AGC based on Equation (4.9).

As a final variable, the total carbon rate, initially estimated for an area of $41m^2$, was extrapolated to a broader region. The measurement was converted from kilograms per square meter to tons per hectare to achieve this. Equation 4.16 illustrates the unit conversion process:

$$AGC_{ha} = \frac{AGC_{41m^2}}{41} \times \frac{10000}{1000}, \tag{4.16}$$

where AGC_{ha} is the AGC in tons (ton) per hectare (ha). Thus, the accessed AGC_{41m^2} value is divided by 41 to achieve a carbon rate in kilograms per quadratic meter. The divided value is subsequently multiplied by 10000 to convert from quadratic meter to hectare, and also is divided per 1000 to convert from kilogram to ton.

Chapter 5

Case Study

The proposed methodology previously presented on Chapter 4 was subsequently implemented on an independent dataset. The objective of the final study was to validate the methodology developed. The results predicted and estimated by previously trained DL algorithms were observed. Only RGB images were used as input data, disregarding labeled numerical values.

5.1 Study Site

The process was carried out in the district of Vilarinho, which is located in the Bragança council, as illustrated in Figure 5.1. The territory of Bragança is also included in the Terras de Trás-os-Montes geographical region, similar to Vimioso council (Figure 4.1). The study was conducted at coordinates $41°53'52.5''$ to $41°54'1.1''N$ and $6°51'10.5''$ to $6°50'53.1''W$.

In addition to analogous climatic and geographical factors, the study region in Vilarinho encompasses exclusively *Pinus pinaster* Ait. colonies. The characterization of the species has been delineated in Section 4.1, in conjunction with the Terras de Trás-os-Montes region.

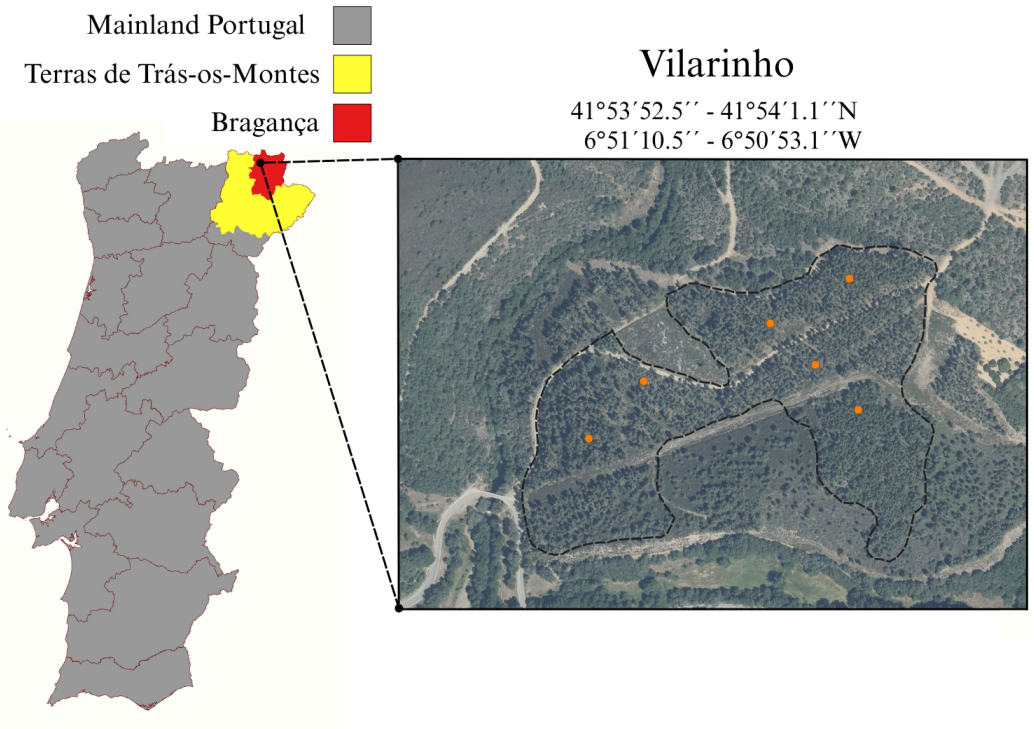

Figure 5.1: Vilarinho study site location.

5.2 Data Acquisition and Comparison

Data acquisition procedures followed the same steps described in Sections 4.2.1 and 4.2.2. Thus, the same materials and devices were employed for acquisition. Defined as ground truth, forest inventory surveys employed the Draudt method to obtain the field data. And the LiDAR data was similar to that obtained by UAV overflight, resulting in raw data configured in point clouds.

The forest inventory surveys were conducted in six sites, starting with field data acquisition. Each plot of interest was situated within a territorial extension of approximately 6.6 *ha* (measured on QGIS software). They were collected in different coordinates, providing more reliable ground truth values for the region. As the total forest area delimitation, the six plots are highlighted in Figure 5.1, considering their center reference.

Table 5.1 shows the measurements manually extracted from each of the six interest

plots, adopting the Draudt method.

Table 5.1: Summarized data from forest survey in Vilarinho applying Draudt method.

Plot	**N° trees**	**Age** [*year*]	**DBH** [*cm*]		**Total height** [*m*]	
			Average	**SD**	**Average**	**SD**
Spot1	15	47	30.7	7.3	20.32	4.86
Spot2	16	47	27.4	8.2	19.31	2.45
Spot3	54	25	16.2	5.7	16.02	2.40
Spot4	20	47	27.1	6.9	21.84	3.31
Spot5	24	47	24.6	6.0	20.14	3.29
Spot6	15	47	30.7	2.6	20.76	1.49

It is possible to highlight some comparisons between São Joanico (Table 4.1) and Vilarinho field data acquisition. Most of the colonies in Vilarinho were aged 47 years old, while in São Joanico, it was estimated as 34. This gap reflects in disparities related to tree dimensions, including its DBH and total height. Table 5.2 briefly summarizes both field data collections.

Table 5.2: Study sites DBH and total height global measurements comparison.

Study site	**DBH** [*cm*]		**Total height** [*m*]	
	Average	**SD**	**Average**	**SD**
São Joanico	23.6	3.5	15.45	2.19
Vilarinho	26.1	5.4	19.73	2.00

However, the methodology employs the total height as ground truth to achieve the *height* by Convolutional Neural Network (CNN) prediction. This scenario encompasses a potential deviation for the *height* variable, considering a previously trained model that only considers São Joanico data. Thus, a total height ratio was established between Vilarinho and São Joanico averages, as shown in Equation (5.1):

$$ratio_{Ht} = \frac{19.73}{15.45} = 1.28, \tag{5.1}$$

where $ratio_{Ht}$ is the ratio between Vilarinho and São Joanico global average for total height. The value of 1.28 summarizes a tendency of individuals 28% taller in Vilarinho related to São Joanico.

Simultaneously, the age discrepancy exhibited no substantial influence on the quantity of trees surveyed in each forest inventory. This suggests that, despite a difference of 13 years between the most representative plots in each study site, their stand densities are similar.

The study [110] analyzed several *Pinus pinaster* Ait. stands, considering different age groups. It was observed that stand densities remained approximately constant between the ages of 35 and 45. The research was conducted in the northern region of Portugal, exhibiting similar climatic factors to the regions studied in this study.

Table 5.3 shows the stand density relative to each interest plot. As well as defined for São Joanico stand densities analysis (Tables 4.9 to 4.11), the lesser representative groups were disregarded. This implies removing Plot *Spot*3 because of its high expected stand density compared to the others (Table 5.1). The stand density situation in Vilarinho is presented by Table 5.3.

Table 5.3: Most representative stand densities of colonies in Vilarinho.

Plot	**Age** [*year*]	**250**m^2			**Hectare**		
		N_{250m^2}	**Average**	**SD**	$N_{hectare}$	**Average**	**SD**
Spot1	47	15			600		
Spot2	47	16			640		
Spot4	47	20	18	≈ 4	800	720	≈ 157
Spot5	47	24			960		
Spot6	47	15			600		

Equation 5.2 shows the average stand in Vilarinho considering an extension of $41m^2$:

$$N_{V\_41m^2} = \frac{720 \times 41}{10000} = \frac{2952}{1000} \approx 3 \; trees, \tag{5.2}$$

where, $N_{V\_41m^2}$ is the estimated number of trees per $41m^2$ in Vilarinho. The same estimate was obtained for the São Joanico study site, as shown in Equation 4.13. This coherence between $N_{SJ\_41m^2}$ and $N_{V\_41m^2}$ estimated values consolidates a similar stand density among both study sites.

Also, the allometric equations were implemented to obtain the total height values for nondominant or sample individuals. Table 5.4 complements the ground truth information, presenting estimated values applying the specific biometric relationships for *Pinus pinaster* Ait.

Table 5.4: Biometric values obtained applying allometric equations.

Plot	**V** $[m^3]$	**AGB** $[kg]$	**AGC** $[kg]$	AGC_{ha} $[t.ha^{-1}]$	**Average** $[t.ha^{-1}]$	**SD** $[t.ha^{-1}]$
Spot1	12.278	6937.330	3468.665	138.75	128.52	10.53
Spot2	10.240	5785.419	2892.710	115.71		
Spot3	10.367	5857.112	2928.556	117.14		
Spot4	12.353	6979.503	3489.752	139.59		
Spot5	11.839	6689.174	3344.587	133.78		
Spot6	11.164	6307.513	3153.757	126.15		

Following field data acquisition, the LiDAR data covered the total study area, encompassing the six forest survey plots. Representing a smaller extension of 6.6 *ha* compared to São Joanico (40 *ha*), the full Vilarinho study site was obtained by one overflight.

After training the model with the São Joanico dataset (Section 4.4), it was only necessary to extract RGB data from the Vilarinho forest region UAV-based LiDAR scan. Thus, just the de RGB raster was extracted from the LiDAR point cloud. Figure 5.2 shows the RGB raster obtained on QGIS software, as described in Section 4.3.2.

In addition to the RGB raster, Figure 5.2 also highlights the six spots of interest.

Yellow squares delimit each forest inventory survey boundary. Meanwhile, the portions of the RGB raster that will be used as red circles surround test data.

Figure 5.2: RGB raster of Vilarinho study site on QGIS.

5.3 Dataset

The geographical coordinates of each forest inventory were employed to extract a local RGB raster with dimensions of 192×192 pixels on QGIS. This procedure resulted in six clipped rasters containing the exact dimensions, as illustrated in Figure 5.3.

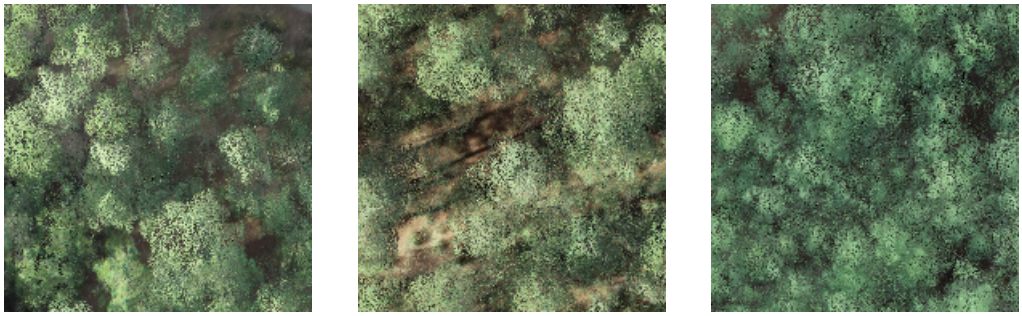

(a) Spot1_RGB.tif (b) Spot2_RGB.tif (c) Spot3_RGB.tif

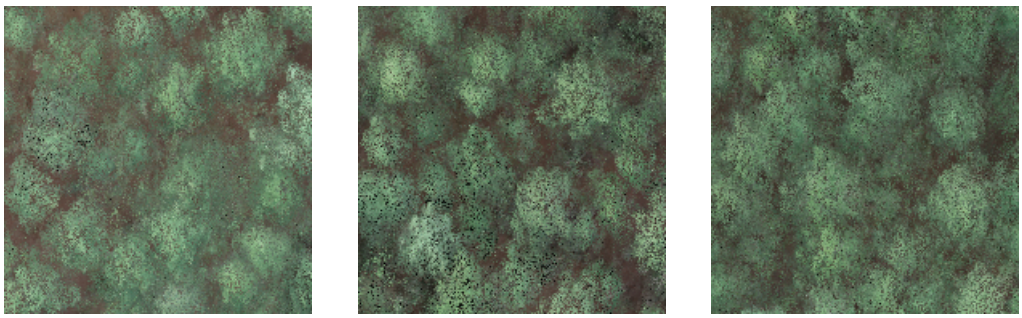

(d) Spot4_RGB.tif (e) Spot5_RGB.tif (f) Spot6_RGB.tif

Figure 5.3: Interest plots of study RGB clipped rasters (Vilarinho).

Adopting the same input dimension of 64×64 pixels by the trained model, each clipped RGB raster provided nine RGB images as samples. A total of 54 samples were obtained from the LiDAR data. This dataset amount was fully allocated for test, considering a previously trained model employing the dataset presented in Section 4.4,

Chapter 6

Results and Discussion

In addition to the best CNN model selection, this chapter presents the test set and results related to each of the two case studies and their respective discussions. Described in Chapter 4, the case of São Joanico will be presented first. Finally, the isolated application case of Vilarinho, as presented in Chapter 5, will be carried out.

6.1 Best Model Selection

During the stage of comparing the performance of each CNN model, Table 6.1 was obtained by establishing the prediction of the "*height*" variable. As delineated in Section 4.5.1, the R^2 metric was the exclusive metric evaluated when selecting the best-fit model for the application. Concurrently, Table 6.2 presents the R^2 values obtained by each model when predicting the "*coverage*" variable.

Table 6.1: Test-phase R^2 values for CNN models predicting "*height*".

CNN model	**Patience parameter set**			
	7	**10**	**15**	**20**
VGG16	0.320	0.266	0.371	0.242
VGG19	0.050	0.391	0.347	0.441
ResNet50	0.087	0.087	0.087	0.144
ResNet152V2	−4.237	−4.237	−3.566	−2.560
MobileNetV2	−138.049	−106.997	−107.001	−106.999
EfficientNet-B7	−11.526	−11.526	−5.702	−0.060

Table 6.2: Test-phase R^2 values for CNN models predicting "*coverage*".

CNN model	**Patience parameter set**			
	7	**10**	**15**	**20**
VGG16	−0.045	0.105	0.352	0.170
VGG19	0.326	0.236	0.451	0.322
ResNet50	−0.243	0.103	0.103	0.246
ResNet152V2	−2.820	−0.750	−0.932	−2.570
MobileNetV2	−0.258	−0.149	−0.279	−0.258
EfficientNet-B7	−0.080	−0.080	−4.229	−0.100

The implementation of all models was carried out applying the *Early Stopping* framework, and any one reached the 100 *epochs* previously adjusted.

Although adequate R^2 values were obtained, ranging from 0 to 1, negative values were also found in implementing specific models. A prevailing tendency of negative values was observed in more complex models, including ResNet152V2, MobileNetV2, and EfficientNet-B7. This phenomenon is presumably associated with the low resolution of the input RGB images. When configured to process more complex images with higher resolutions (typically 224×224 or 600×600 pixels), this expectation divergence can lead to model performance disparities.

As demonstrated in Equation (3.5), an analysis of the mathematical description of R^2 reveals that negative values of a relatively low magnitude indicate the prediction of the average between the ground-truth values of the input data.

This scenario demonstrates non-optimal performance, as the model disregards the prediction of variables. Conversely, the model is converging its predictions to a narrow range

of values, the average between the labeled values. Table 6.3 shows the "*height*" variable prediction results obtained by the EficcientNet-B7 model ($R^2 = -0.060$), displaying the behavior described.

Table 6.3: Typical behavior observed for models with low negative R^2 values.

filename	**Ground-truth** $[m]$	***height*** $[m]$	**MAE** $[m]$	**MSE** $[m]$	**RMSE** $[m]$
five_0_0.png	14.91	15.39			
three_0_1.png	12.95	15.36			
six_0_2.png	16.02	15.33			
one_1_0.png	12.78	15.32	2.2×10^0	6.7×10^0	2.6×10^0
four_1_1.png	14.57	15.36			
seven_1_2.png	18.51	15.33			
eight_2_0.png	17.52	15.35			
nine_2_1.png	20.37	15.35			

Table 6.4: Typical behavior observed for models with high negative R^2 values.

filename	**Ground-truth** $[m]$	***height*** $[m]$	**MAE** $[m]$	**MSE** $[m]$	**RMSE** $[m]$
five_0_0.png	14.91	45.19			
three_0_1.png	12.95	46.95			
six_0_2.png	16.02	45.98			
one_1_0.png	12.78	45.82	2.9×10^1	8.8×10^2	3.0×10^1
four_1_1.png	14.57	46.71			
seven_1_2.png	18.51	44.16			
eight_2_0.png	17.52	42.08			
nine_2_1.png	20.37	46.37			

In contrast, higher R^2 values exhibited greater instability. The analysis revealed no consistent tendency among models with the highest negative values to predict local or

average values. As illustrated in Table 6.4, the MobileNetV2 model ($R^2 = -138.049$) demonstrated a dispersed behavior when predicting the "*height*" variable.

While the model does tend to predict values within a defined interval, this range is significantly offset from the average ground-truth values. A comparison of the performance metrics in Table 6.3 reveals a notable increase in the MAE, MSE, and RMSE, indicating a greater degree of instability in models with higher R^2 values.

Given the observed behavior depicted in Tables 6.3 and 6.4, it is reasonable to disregard the ResNet152V2, MobileNetV2, and EfficientNet-B7 models. Table 6.5 highlights the best-performing structures, indicating their positive R^2 values, during the most suitable model selection stage.

Table 6.5: Test-phase positive R^2 values for best-performing CNN models.

Variable	**Patience parameter set**	**VGG16**	**VGG19**	**ResNet50**
height	7	0.320	0.050	0.087
	10	0.266	0.391	0.087
	15	0.371	0.347	0.087
	20	0.242	0.441	0.144
coverage	7	–	0.326	–
	10	0.105	0.236	0.103
	15	0.352	0.451	0.103
	20	0.170	0.322	0.246

Despite the predominantly positive R^2 values, the ResNet50 model manifested patterns of insensitivity to variations in the patience parameter. The constant values of 0.087 and 0.103 for R^2 reflect the possible saturation of the model during its establishment. This suggests that ResNet50 was not well-suited to the task, which supports the model rejection.

The Visual Geometric Group (VGG) architecture displayed the optimal learning performance, as determined by the R^2 metric analysis. The VGG16 model demonstrated

favorable R^2 values, suggesting acceptable performance. However, the model also exhibited a negative value when predicting the "*coverage*" variable, with patience set to 7. This finding points to an unstable reaction by VGG16 to the analysis criteria imposed.

The VGG19 model, in addition to its absence of negative R^2 values, revealed enhanced consistency when considering variations in patience values. VGG19 demonstrated the highest R^2 values among all the models employed. The optimal performances resulted in 0.441 and 0.451 for predicting the "*height*" and "*coverage*" variables, respectively. Notably, these results were obtained for different values of patience, as illustrated in Table 6.5.

Table 6.6 presents the evaluation metrics obtained during the implementation of the VGG19 model, highlighting the optimal performance achieved during the selection stage.

Table 6.6: Complete evaluating metrics set applied to the VGG19 model.

Variable	**Split set**	**MAE** $[m\ ;\ \%]$	**MSE** $[m\ ;\ \%]$	**RMSE** $[m\ ;\ \%]$	R^2
height	k-fold 1	2.4×10^{0}	9.1×10^{0}	3.0×10^{0}	0.022
	k-fold 2	2.0×10^{0}	5.9×10^{0}	2.4×10^{0}	0.043
	k-fold 3	1.2×10^{0}	2.8×10^{0}	1.7×10^{0}	0.286
	k-fold 4	2.8×10^{0}	9.5×10^{0}	3.1×10^{0}	0.029
	k-fold 5	1.7×10^{0}	4.9×10^{0}	2.2×10^{0}	0.356
	test	1.4×10^{0}	3.5×10^{0}	1.9×10^{0}	0.441
coverage	k-fold 1	2.3×10^{-1}	7.1×10^{-2}	2.7×10^{-1}	0.004
	k-fold 2	9.2×10^{-2}	1.2×10^{-2}	1.1×10^{-1}	0.635
	k-fold 3	1.3×10^{-1}	2.8×10^{-2}	1.7×10^{-1}	0.152
	k-fold 4	1.4×10^{-1}	3.6×10^{-2}	1.9×10^{-1}	0.018
	k-fold 5	1.2×10^{-1}	2.3×10^{-2}	1.5×10^{-1}	0.340
	test	1.3×10^{-1}	2.4×10^{-2}	1.5×10^{-1}	0.451

6.2 Case Study: São Joanico

This section aims to present a continuation of the trained VGG19 model applying only São Joanico data. Section 4.4 previously described about this introductory stage. Thus, it direct follows the training/validation phase presented in Section 6.1.

6.2.1 Test set

The test set for São Joanico case study was composed of 8 samples, randomly selected from 81. Figure 6.1 displays the RGB images that make up this set, while Table 6.7 shows their respective "*height*" and "*coverage*" values. The remaining 73 samples were applied to the training/validation set, as established in Section 4.4.5.

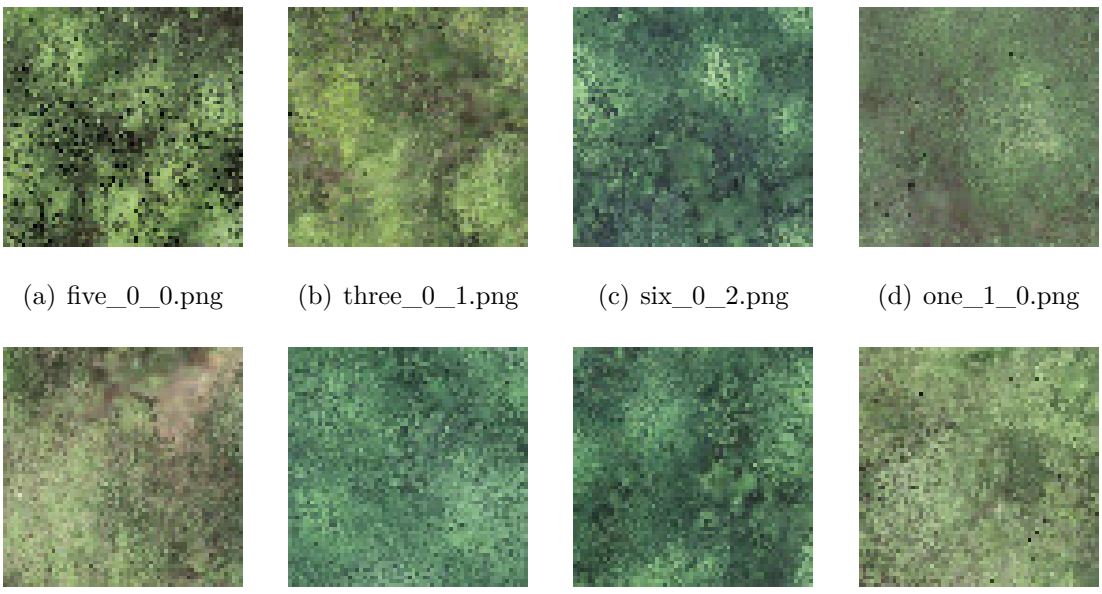

(a) five_0_0.png (b) three_0_1.png (c) six_0_2.png (d) one_1_0.png

(e) four_1_1.png (f) seven_1_2.png (g) eight_2_0.png (h) nine_2_1.png

Figure 6.1: Randomly assigned RGB images for test set.

Table 6.7: Test set *filename*, *height* and *coverage* labels.

filename	***height*** $[m]$	***coverage*** [%]
five_0_0.png	14.91	0.973
three_0_1.png	12.95	0.583
six_0_2.png	16.02	0.405
one_1_0.png	12.78	0.519
four_1_1.png	14.57	0.587
seven_1_2.png	18.51	0.912
eight_2_0.png	17.52	0.597
nine_2_1.png	20.37	0.964

6.2.2 Results

Table 6.8 shows the predicted variables, such as the dependent variables, for each São Joanico test sample, which includes:

- "*height*" has described in Section 4.3.1;
- "*DBH*" has described in Equation 4.14;
- "*coverage*" has described in Section 4.4.2;
- "*N° trees*" has described in Table 4.12.

Table 6.8: Predicted variables and their dependents by VGG19 for São Joanico.

filename	***height*** $[m]$	**DBH** $[cm]$	***coverage*** $[\%]$	**N° trees**
five_0_0.png	16.08	26.4	0.798	4
three_0_1.png	14.86	24.4	0.639	3
six_0_2.png	15.53	25.5	0.574	3
one_1_0.png	13.31	21.4	0.445	3
four_1_1.png	14.53	23.8	0.631	3
seven_1_2.png	16.62	27.2	0.666	3
eight_2_0.png	16.61	27.2	0.643	3
nine_2_1.png	16.08	26.4	0.725	4

Previously, Table 4.1 presented the ground truth values obtained from the study plots in the field. The average total height ranged from 11.87 to 18.19 m, while the DBH ranged from 17.0 to 27.5 cm.

In consideration of the "*height*" variable (Table 6.8), the predicted total heights ranged from 13.31 to 16.62 m. These limits fall entirely within the range obtained from the ground truth values. This scenario demonstrates that the "*height*" variable was adequately predicted, falling within the validation interval.

Figure 6.2 illustrates the relationship between ground truth and predicted *heights* values. The border lines were obtained considering the average values of total height about each of the nine spots, showing an SD of 2.19 m.

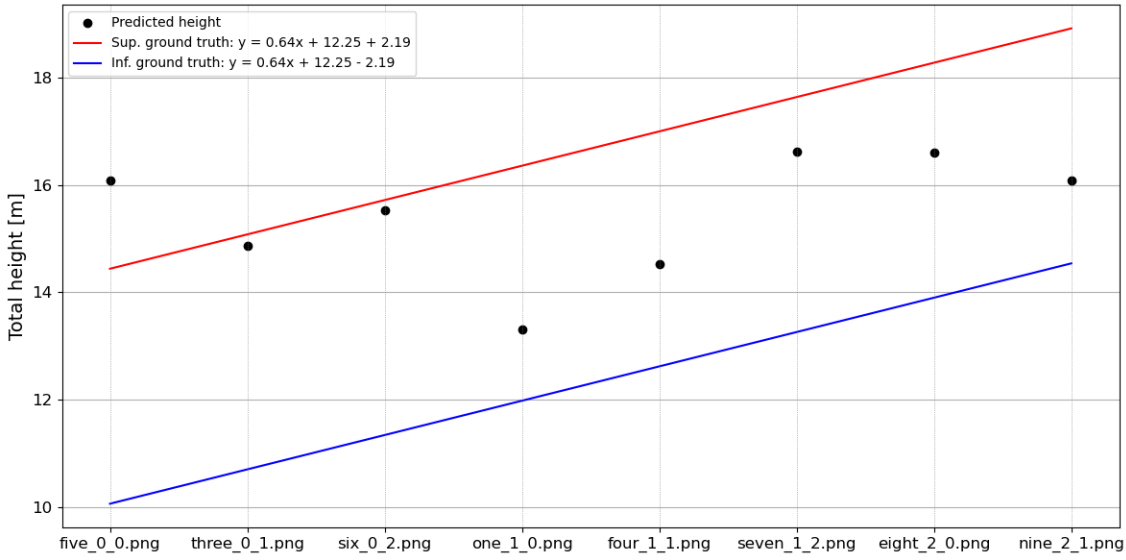

Figure 6.2: Predicted values of *height* related with ground truth interval (São Joanico).

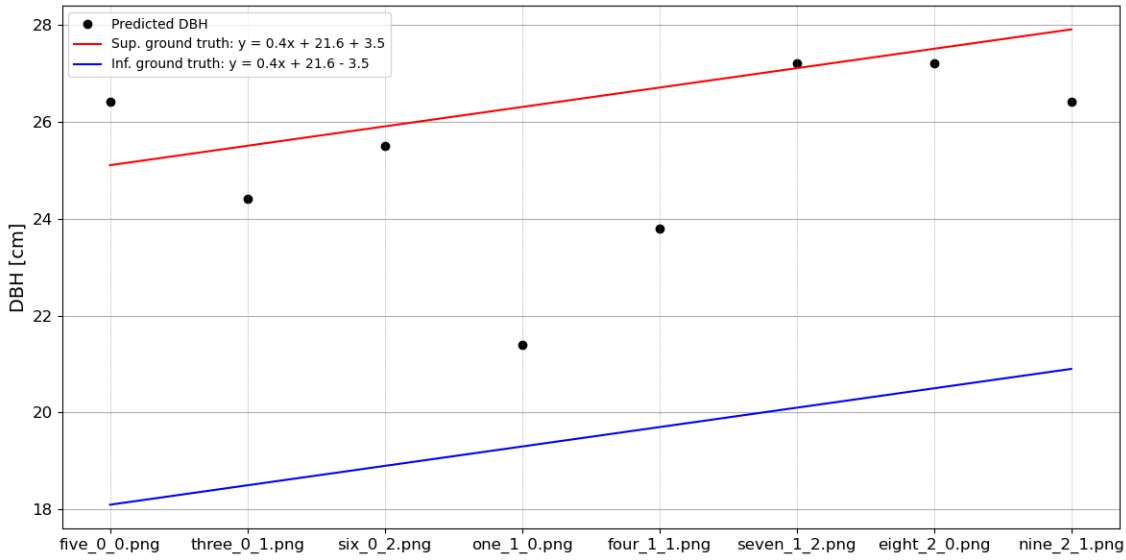

Figure 6.3: Predicted values of DBH related to ground truth interval (São Joanico).

The "DBH" variable yielded estimated values ranging from 21.4 to 27.2 *cm*. However, they also fell within their respective ground truth intervals of 17.0 to 27.5 *cm*. A greater approximation to the upper limit was observed, since no value below 21.4 *cm* was estimated. Similar results were obtained for *height* prediction. Figure 6.3 shows the

relationship of the DBH variable.

In parallel, Table 4.1 has introduced the number of trees at each interest plot from field data. As shown in Equation 4.13, these values reflected stand densities of approximately three trees per $41m^2$. Following the findings in Table 4.1, Table 4.9 supported the hypothesis that a subset of samples may exhibit "N° trees" values exceeding 3.

This dynamic is evidenced by the behavior of the "N° trees" variable, as shown in Table 6.8. Related with the "*coverage*" variable, the "N° trees" values converged on a number of 3 (Equation 4.13). Furthermore, two samples exhibited a value of 4, corresponding to the ground truth background outlined in Tables 4.1 and 4.9.

The final target variables were also achieved after obtaining the first variables (Table 6.8). Table 6.9 shows the final variables obtained for each test sample, including:

- "AGB" has described in Equation 4.7;
- "V" has described in Equation 4.2;
- "ρ_b", or "tree_density", has described in Equation 4.8;
- "AGC" has described in Equation 4.9.

Table 6.9: Obtained variables linked with their relative predictions (São Joanico).

filename	**AGB** $[kg]$	**V** $[m^3]$	**tree_density** $[kg.m^{-3}]$	**AGC** $[kg]$
five_0_0.png	229.573	0.444	517.231	114.786
three_0_1.png	182.966	0.355	515.836	91.483
six_0_2.png	208.439	0.403	516.596	104.219
one_1_0.png	126.439	0.246	514.132	63.220
four_1_1.png	170.603	0.331	515.467	85.302
seven_1_2.png	250.676	0.484	517.875	125.338
eight_2_0.png	250.305	0.483	517.864	125.153
nine_2_1.png	229.799	0.444	517.238	114.899

As mentioned in 4.1, the *Pinus pinaster* Ait. species has a density typically ranging from 461 to $660kg.m^{-3}$. Table 1 demonstrates that the obtained tree densities ranged

from 514.132 to 517.875$kg.m^{-3}$. This matching substantiates the notion that allometric equations were used appropriately to achieve biomass (AGB) and phytovolume (V) estimations.

With the results presented in Tables 6.8 and 6.9, the final variables for each sample in the test set were obtained. Table 6.10 shows the final results obtained, including:

- "AGC_{41m^2}" has described in Equation 4.15;
- "AGC_{ha}" has described in Equation 4.16.

Table 6.10: Obtained variables linked with carbon measurements (São Joanico).

filename	AGC_{41m^2} $[kg]$	AGC_{ha} $[t.ha^{-1}]$	**Average** $[t.ha^{-1}]$	**SD** $[t.ha^{-1}]$
five_0_0.png	459.145	111.99	82.40	23.64
three_0_1.png	274.450	66.94		
six_0_2.png	312.658	76.26		
one_1_0.png	189.659	46.26		
four_1_1.png	255.905	62.42		
seven_1_2.png	376.014	91.71		
eight_2_0.png	375.458	91.57		
nine_2_1.png	459.598	112.10		

From the ground truth values, an average rate of 75.18$t.ha^{-1}$ was obtained (Table 4.2) for the study region. The value of 14.57$t.ha^{-1}$ was obtained as this measurement's SD.

As shown in Table 6.10, an average rate of 82.40$t.ha^{-1}$ was achieved considering the predicted and estimated values. With an absolute error of 7.22$t.ha^{-1}$ based on ground truth, this result reflects a tolerance of 9%. Given a slight difference of approximately 7$t.ha^{-1}$ between the two rates, it is feasible to attribute a certain degree of reliability to the predicted value.

However, a notable increase in the predicted carbon rate was recorded. The SD of the predicted rate was found to be 23.64$t.ha^{-1}$, while the ground truth rate yielded a value of 14.57$t.ha^{-1}$.

This disparity can be explained by the different dimensions considered during the two stages. It is anticipated that the 250m^2 dimensions of the ground truth analyses represent

the study region more robustly than the $41m^2$ dimensions of the prediction samples. This variability may be mitigated by enhancing the quantity of predictions, thus offering a broader representation of the study region.

Given the predicted carbon rate of $82.40t.ha^{-1}$, it is possible to estimate the amount of carbon sequestration storage in the $40ha$ extension forest area under analysis. Equation 6.1 elucidates the carbon stock achievement within the São Joanico case.

$$C_{SJ} = 82.40 \times 40 = 3296 \pm\ 288.80\ tons, \tag{6.1}$$

where C_{SJ} is the estimated carbon sequestration amount of 3296 *tons* in São Joanico study site. According to the field data, this estimate implies a tolerance of approximately 9%, adopted as ground truth.

6.3 Case Study: Vilarinho

Following the precise results achieved in São Joanico, Vilarinho case study was introduced as a manner to consolidate the methodology developed. This is the main justification for the absence of Vilarinho data during the VGG19 model establishment. As an isolated application case, the context of Vilarinho was separated described in Chapter 5.

6.3.1 Test set

In contrast to the São Joanico case, the dataset of Vilarinho disregarded numerical labeled values, as pointed in Section 5.3. Only the identification label *filename* was attributed to the samples. Thus, the complete methodology application in Vilarinho was conducted to simulate the most realistic scenario.

The Vilarinho dataset was used exclusively for testing, employing the algorithm previously trained with São Joanico data (Section 6.1). A total of 54 test samples were obtained from the six 192×192 RGB rasters presented in Figure 5.3.

6.3.2 Results

Initially, no additional adjustments were applied to the established test set. Table 6.11 shows the predicted *height* within its estimated DBH values, encompassing the obtained individuals dimension for the Vilarinho application case.

Table 6.11: Predicted dimension values by VGG19 for Vilarinho case.

Samples	***height*** $[m]$		**DBH** $[cm]$	
	Average	**SD**	**Average**	**SD**
Spot1	15.73	1.09	25.6	2.5
Spot2	16.08	0.86	26.3	1.3
Spot3	16.35	0.80	26.7	1.1
Spot4	14.83	0.51	24.3	0.9
Spot5	15.12	0.52	24.8	0.9
Spot6	14.91	0.61	24.5	1.1
Amount	15.50	1.02	25.4	1.6

Table 5.1 previously delineated the range of 16.02 to 21.84m as the ground truth for *height* values related to Vilarinho. In contrast to the analysis in São Joanico, most of the predicted data from Vilarinho deviated from the ground truth range. Including the global average, with the value of 15.5m showing a standard deviation of 1.02m, indicating reliability of the deviated value.

On the other hand, DBH values were within the ground truth range, established by the limits of 16.2 to 30.7cm. This supports that DBH does not differ significantly as total height between the two forest areas, as shown in Table 5.2.

The rough disparity by *height* values is reflected in several deviations of the dependent variables. Considering the following estimations, these adverse effects were better highlighted within the *coverage* variable predictions.

An average value of 84.73$t.ha^{-1}$ was achieved for the carbon rate, with a SD of 25.35$t.ha^{-1}$. Meanwhile, 321.30$t.ha^{-1}$ was ground truth. Indicating a numerical gap of almost 240$t.ha^{-1}$, this initial attempt was disregarded considering carbon sequestration analysis in Vilarinho.

However, the procedure was once again implemented, applying $ratio_{Ht}$ (Equation 5.1)

as *height* variable normalization parameter. Tables 6.12 and 6.13 present the predicted variables, considering a percent normalization of 28% for *height* values.

Table 6.12: Predicted variables and its dependents by VGG19 for Vilarinho (I).

filename	***height*** $[m]$	**DBH** $[cm]$	***coverage*** $[\%]$	**N° trees**
one_0_0.png	19.59	30.1	0.836	4
one_0_1.png	18.06	28.8	0.549	3
one_0_2.png	17.25	28.0	0.538	3
one_1_0.png	20.79	30.6	0.674	3
one_1_1.png	22.61	30.8	0.673	3
one_1_2.png	17.94	28.7	0.598	3
one_2_0.png	18.15	28.9	0.695	3
one_2_1.png	23.32	30.7	0.810	4
one_2_2.png	22.15	30.8	0.678	3
two_0_0.png	20.20	30.4	0.688	3
two_0_1.png	19.83	30.2	0.755	4
two_0_2.png	19.61	30.1	0.822	4
two_1_0.png	19.59	30.1	0.718	4
two_1_1.png	22.12	30.8	0.823	4
two_1_2.png	18.83	29.5	0.769	4
two_2_0.png	21.06	30.7	0.838	4
two_2_1.png	21.76	30.8	0.764	4
two_2_2.png	20.75	30.6	0.784	4
three_0_0.png	18.90	29.6	0.675	3
three_0_1.png	23.52	30.6	0.762	4
three_0_2.png	18.67	29.4	0.711	4
three_1_0.png	22.35	30.8	0.760	4
three_1_1.png	21.23	30.8	0.698	3
three_1_2.png	20.42	30.5	0.782	4
three_2_0.png	20.70	30.6	0.714	4
three_2_1.png	20.35	30.5	0.726	4
three_2_2.png	19.10	29.7	0.791	4

The normalized implementation pointed a better adjusted performance between ground truth (16.02 to 21.84 m) and predicted values for Vilarinho case. The *height* predicted values ranged from 17.00 to 23.52 m, with an average value of 19.40 m. An average increase of 3.90 m was delineated compared to the previously attempted implementation (Table 6.11). Thus, is possible to confirm that $ratio_{Ht}$ parameter provided best suited predictions related to total heights in Vilarinho.

Table 6.13: Predicted variables and its dependents by VGG19 for Vilarinho (II).

filename	***height*** $[m]$	**DBH** $[cm]$	***coverage*** $[\%]$	**N° trees**
four_0_0.png	17.71	28.5	0.569	3
four_0_1.png	18.04	28.8	0.680	3
four_0_2.png	18.10	28.9	0.594	3
four_1_0.png	17.64	28.4	0.652	3
four_1_1.png	17.32	28.0	0.557	3
four_1_2.png	18.41	29.2	0.660	3
four_2_0.png	18.31	29.1	0.647	3
four_2_1.png	18.69	29.4	0.621	3
four_2_2.png	17.57	28.3	0.493	3
five_0_0.png	17.88	28.7	0.676	3
five_0_1.png	17.50	28.3	0.606	3
five_0_2.png	17.79	28.6	0.570	3
five_1_0.png	20.15	30.4	0.695	3
five_1_1.png	20.55	30.6	0.661	3
five_1_2.png	17.87	28.7	0.545	3
five_2_0.png	18.66	29.4	0.688	3
five_2_1.png	18.86	29.6	0.735	4
five_2_2.png	17.31	28.0	0.599	3
six_0_0.png	18.31	29.1	0.668	3
six_0_1.png	19.23	29.8	0.669	3
six_0_2.png	17.00	27.7	0.524	3
six_1_0.png	18.77	29.5	0.585	3
six_1_1.png	17.79	28.6	0.625	3
six_1_2.png	20.22	30.4	0.688	3
six_2_0.png	17.12	27.8	0.454	3
six_2_1.png	21.54	30.8	0.691	3
six_2_2.png	20.59	30.6	0.680	3

Figure 6.4 ensures the interval encompasses the relationship between ground truth and predicted values of *height*. In contrast to Figures 6.2 and 6.3, instead of the spots' average values, all extracted values from the ground truth were considered to achieve the border lines. This was decided to validate a different comparison between the values' natures, and explain the lesser inclination behavior by the lines.

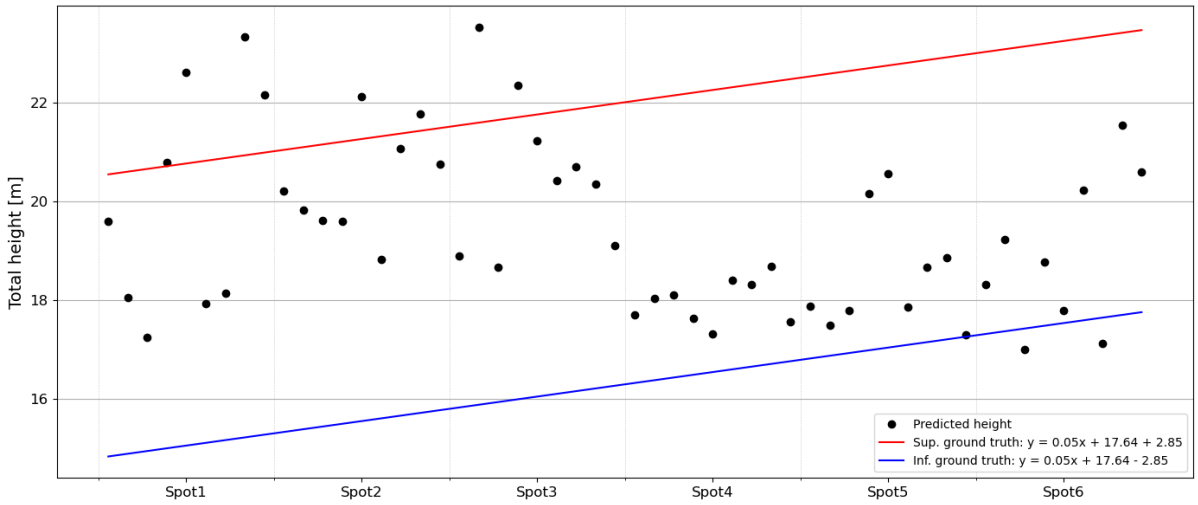

Figure 6.4: Predicted values of *height* related with ground truth interval (Vilarinho).

Once *height* direct influences DBH variable, is reasonable to check again its response to the model predictions. The lowest estimated DBH value obtained was 27.7 *cm* while the highest reached 30.8 *cm*, defining an average of 29.6 *cm*. This interval is also encompassed by the ground truth range (16.2 to 30.7 *cm*), as achieved in the nonnormalized attempt.

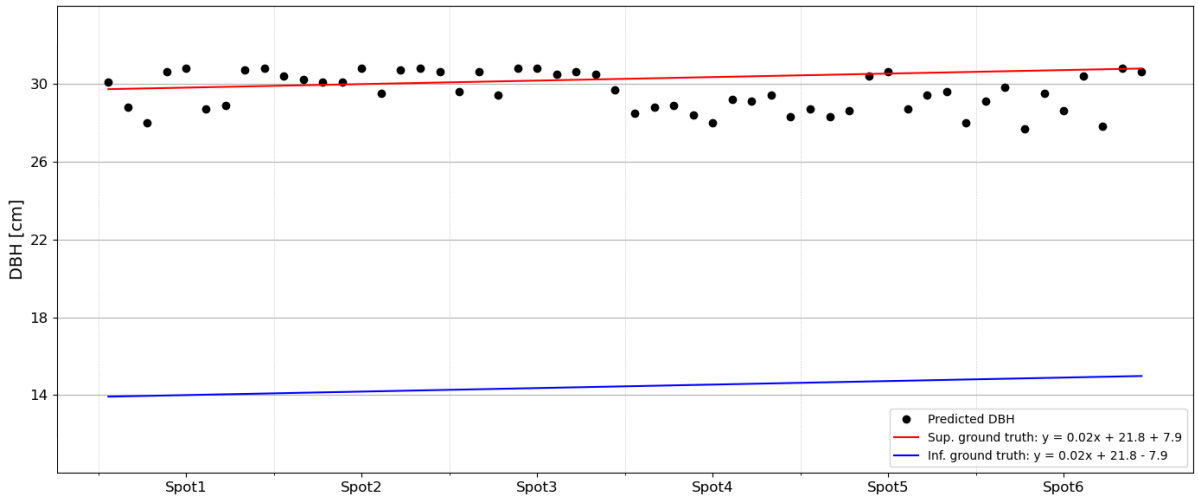

Figure 6.5: Predicted values of DBH related to ground truth interval (Vilarinho).

Figure 6.5 shows the obtained DBH values behavior related to its ground truth values. It can be seen that the application of the $ratio_{Ht}$ almost influenced the exclusion of the

estimated DBH values from their respective ground truth interval.

Analyzing "N° trees" variable, 36 samples obtained the quantity of 3 trees while the remaining 18 pointed to 4. This scenario supports the ground truth foundation, in Equation 5.2. Samples that achieved 4 to "N° trees" also represent feasibility in the Vilarinho case. This is explainable by the presence of some colonies with higher expected stand density, as the 25 age colony by *Plot*3 (Table 5.1).

Meanwhile, integral absence for values of 2 trees for "N° trees" variable is also questionable, once it is also possible to reach (Table 4.12). Even considering a relative higher test volume for Vilarinho case, any sample showed "N° trees" variable equal to 2. This indicates that the model doesn't obtain sufficient samples with *coverage* label below 0.3 during training and validation.

Once the dimension values obtained were acceptable, Vilarinho proceeded with the analysis. Table 6.14 presents the estimated biometric values, grouped by their respective plots and the number of results.

Table 6.14: Obtained variables linked with their relative predictions (Vilarinho).

Samples	**AGB** $[kg]$	**V** $[m^3]$	**tree_density** $[kg.m^{-3}]$	**AGC** $[kg]$
Spot1	355.611	0.680	522.527	177.806
Spot2	376.351	0.720	522.923	188.176
Spot3	376.970	0.720	523.283	188.485
Spot4	301.037	0.579	519.526	150.518
Spot5	317.986	0.611	520.250	158.993
Spot6	330.982	0.635	520.892	165.491
Amount	343.156	0.658	521.567	171.578

The higher tree dimension in Vilarinho influenced slight increases in AGB and phytovolume (V) estimations. Considering these variables, Table 6.9 indicates an average of approximately $206kg$ and $0.4m^3$ for each individual in São Joanico. Thus, the trees in Vilarinho study site have AGB and phytovolume values 65% higher than São Joanico.

Once the dimensions are most significant, a tree density increase is also expected. This increase can also be observed in the Vilarinho case which pointed an average of

$521.567 kg.m^{-3}$ while any sample reached the mark of $518 kg.m^{-3}$ for São Joanico. However, the density values obtained for Vilarinho are also encompassed by the typical species tree density range.

As final results of this study, Table 6.15 shows the carbon variables and rate obtained for the application case in Vilarinho.

Table 6.15: Obtained variables linked with carbon measurements (Vilarinho).

Samples	AGC_{41m^2} $[kg]$	AGC_{ha} $[t.ha^{-1}]$	**Average** $[t.ha^{-1}]$	**SD** $[t.ha^{-1}]$
Spot1	577.084	140.75	140.88	35.04
Spot2	731.965	178.53		
Spot3	713.250	174.98		
Spot4	451.555	110.14		
Spot5	495.419	120.83		
Spot6	496.473	121.09		

Previously, the average rate of $128.52 t.ha^{-1}$ for carbon rate was obtained as ground truth for Vilarinho (Table 5.4). Related to the estimated value of $140.88 t.ha^{-1}$, the equal tolerance of approximately 9% (an absolute error of $12.36 t.ha^{-1}$) was obtained, such as in São Joanico case. Equation 6.2 achieves the carbon sequestration amount related to the $6.6 ha$ forest area in Vilarinho:

$$C_V = 140.75 \times 6.6 = 929.81 \pm 81.56 \; tons, \tag{6.2}$$

where C_V is the estimated carbon sequestration amount of 929.81 $tons$ in Vilarinho study site. According to the field data, this estimate implies a tolerance of approximately 9%, adopted as ground truth.

However, a superior SD of $35.04 t.ha^{-1}$ was obtained, while in São Joanico this same estimate was pointed to $23.64 t.ha^{-1}$. This gap indicates a lower reliability for the carbon rate estimated for Vilarinho compared to São Joanico. With a larger test set volume, the opposite situation was more expected.

The necessary normalization procedure for Vilarinho adopting the $ratio_{Ht}$ parameter is a potential factor in answer to this reliability loss. A normalization procedure encompasses

more vulnerability for estimated values, even preceding a consolidated establishment, evidenced in Table 5.2.

The model training and validation set, containing exclusively São Joanico data, required the normalization scenario, decreasing the reliability of the results for Vilarinho. Although achieving a similar tolerance value was possible, it reflected credibility for the methodology applied.

Chapter 7

Conclusions and Future Works

This chapter outlines the final considerations that have emerged from the report carried out. The significance and feasibility of the methodology developed are highlighted. Its confirmation as a robust technique is evidenced by its results, which are also summarized.

Despite ensuring success in an isolated application case, potential areas for further exploration are presented. Finally, frameworks for performance optimization and extending the reach of the methodology will also be suggested as research themes for future works. In addition, related researches developed within the main theme of this work are also presented.

7.1 Conclusions

This work researched the development of an innovative methodology for the remote monitoring of vegetation cover. Data was acquired using a UAV-based LiDAR setup flying over the scanning regions. The study was conducted in two different *Pinus pinaster* Ait. (maritime pine) forests in the northern region of mainland Portugal.

Once the LiDAR data had been obtained, the raw point cloud (.las) data was processed in the QGIS virtual environment. The LAStools extension was used to extract the elevation and image information relevant to this study. The processed data was configured into labels and stored in a single dataset for implementation in CNN algorithms.

Of the six different CNN structures, the VGG19 model exhibited the best learning performance. R^2 scores of 0.441 and 0.451 were achieved during the prediction stage for the *height* and *coverage* variables, respectively. Next, test data related to the same set employed to train the model was used for prediction. With the model already trained, a set of data from another region was only obtained for testing.

Although it estimated several variables, such as DBH, phytovolume and AGB, the study focused on carbon sequestration as the main target variable. In the first case of study (São Joanico), a carbon sequestration rate of $82.40t.ha^{-1}$ was obtained, compared to a ground truth value of $75.18t.ha^{-1}$. For the second situation (Vilarinho), a higher rate of $140.88t.ha^{-1}$ was estimated, with a ground truth value of $128.52t.ha^{-1}$.

Finally, carbon sequestration in two different regions was successfully surveyed. A total area of 46.6 *hectares* was covered, showing a total of 4225.81 *tons* of carbon with a tolerance of 9%. These results highlight the effectiveness of the procedure for accessing vegetation cover. It demonstrates that large areas can be found in a short space of time with a satisfactory margin of error.

7.2 Future Works

Despite the convergence between ground truth and estimated stand densities, the predicted variable *coverage* presented adjustment issues. For example, the absence of predicted values below 0.3. The procedure importance of *coverage* variable can be achieved by other approaches. Techniques for canopy delimitation, such as filter implementation, may provide better individuals identification by canopy delimitation.

Generalization improvements can be reached exploring the implementation of more diverse dataset for algorithms training and validation. Merging samples from different sites is a viable approach to wide range of prediction keeping precision, or even increasing it. This could also mitigate loss by normalization procedures, such as observed after applying $ratio_{Ht}$ parameter.

An oak and pine species were already investigated, achieving promising results. Despite exploring other types, mixed colonies must also be analyzed. This set encompasses a more common scenario, once forests with various species are often present in larger scales than controlled tree areas.

In order to achieve carbon sequestration within extensive areas, other imagery resources should be investigated to RGB images acquiring. Same as satellites, orthophotomaps also covers larger areas, in addition to employs more refined resolutions. This aspect shows a greater feasibility to orthophotomaps than satellite imagery as test samples, and must be better researched.

7.3 Publications

During the development of this master thesis, parallel researches were conducted. Two titles are directly related to the study aims, they are:

> **Britto, R. D.**, Mendes, J., Grilo, V., Castro, J. P., Santos, M.F., Castro, M., Pereira, A. I., and Lima. J., "A Deep Learning Approach for Average Height Estimation in Oak Colony Using RGB Images", *5th International Conference on Optimization, Learning Algorithms and Applications - OL2A*. Genoa, Italy, 2025.

The following article was accepted and will be presented soon:

> **Britto, R. D.**, Mendes, J., Santos, M.F., Castro, J. P., Lima. J., , and Pereira, A. I. "An Artificial Intelligence Method for Large Forest Areas Analysis", *5th Symposium of Applied Science for Young Researchers - SASYR*. Viana do Castelo, Portugal, 2025.

7.4 Fundings

The success of this work was only achieved with the resources provided by two projects, they are:

iCarbono, *Research Centre in Digitalization and Intelligent Robotics - CeDRI* (UID/05757). Fundação La Caixa, PL23-00038.

The following project also supported this work:

LIFE SILFORE, *Mountain Research Center - CIMO* (UIDP/00690/2020). LIFE21-CCA-ES-LIFE.

Bibliography

[1] M. Romanello, C. Di Napoli, C. Green, *et al.*, "The 2023 report of the lancet countdown on health and climate change: The imperative for a health-centred response in a world facing irreversible harms," *The Lancet*, vol. 402, no. 10419, pp. 2346–2394, 2023.

[2] T. E. Avery and H. E. Burkhart, *Forest measurements*. Waveland Press, 2015.

[3] F. Islam, M. Nabi, and J. E. Ball, "Off-road detection analysis for autonomous ground vehicles: A review," *Sensors*, vol. 22, no. 21, p. 8463, 2022.

[4] F. A. Ruetz, N. Lawrance, E. Hernández, P. V. Borges, and T. Peynot, "Forest-trav: 3d lidar-only forest traversability estimation for autonomous ground vehicles," *IEEE Access*, vol. 12, pp. 37 192–37 206, 2024.

[5] V. Karjalainen, N. Koivumäki, T. Hakala, *et al.*, "Towards autonomous photogrammetric forest inventory using a lightweight under-canopy robotic drone," *arXiv preprint arXiv:2501.12073*, 2025.

[6] J. Paneque-Gálvez, M. K. McCall, B. M. Napoletano, S. A. Wich, and L. P. Koh, "Small drones for community-based forest monitoring: An assessment of their feasibility and potential in tropical areas," *Forests*, vol. 5, no. 6, pp. 1481–1507, 2014.

[7] J. P. Dandois and E. C. Ellis, "High spatial resolution three-dimensional mapping of vegetation spectral dynamics using computer vision," *Remote Sensing of Environment*, vol. 136, pp. 259–276, 2013.

[8] S. A. H. Mohsan, M. A. Khan, F. Noor, I. Ullah, and M. H. Alsharif, "Towards the unmanned aerial vehicles (uavs): A comprehensive review," *Drones*, vol. 6, no. 6, p. 147, 2022.

[9] N. Guimarães, L. Pádua, P. Marques, N. Silva, E. Peres, and J. J. Sousa, "Forestry remote sensing from unmanned aerial vehicles: A review focusing on the data, processing and potentialities," *Remote Sensing*, vol. 12, no. 6, p. 1046, 2020.

[10] X. Liang, V. Kankare, J. Hyyppä, *et al.*, "Terrestrial laser scanning in forest inventories," *ISPRS Journal of Photogrammetry and Remote Sensing*, vol. 115, pp. 63–77, 2016.

[11] Y. Guo, H. Wang, Q. Hu, H. Liu, L. Liu, and M. Bennamoun, "Deep learning for 3d point clouds: A survey," *IEEE transactions on pattern analysis and machine intelligence*, vol. 43, no. 12, pp. 4338–4364, 2020.

[12] A. Krizhevsky, I. Sutskever, and G. E. Hinton, "Imagenet classification with deep convolutional neural networks," *Advances in neural information processing systems*, vol. 25, 2012.

[13] S. Beck and M. Mahony, "The ipcc and the new map of science and politics," *Wiley Interdisciplinary Reviews: Climate Change*, vol. 9, no. 6, e547, 2018.

[14] R. K. Pachauri, A. Reisinger, *et al.*, "Ipcc fourth assessment report," *IPCC, Geneva*, vol. 2007, no. 673, p. 044 023, 2007.

[15] C. Fetting, "The european green deal," *ESDN Report, December*, vol. 2, no. 9, p. 53, 2020.

[16] S. Wolf, J. Teitge, J. Mielke, F. Schütze, and C. Jaeger, "The european green deal—more than climate neutrality," *Intereconomics*, vol. 56, pp. 99–107, 2021.

[17] G. Reiersen, D. Dao, B. Lütjens, *et al.*, "Reforestree: A dataset for estimating tropical forest carbon stock with deep learning and aerial imagery," in *Proceedings of the AAAI Conference on Artificial Intelligence*, vol. 36, 2022, pp. 12 119–12 125.

[18] F. Zhang, X. Tian, H. Zhang, and M. Jiang, "Estimation of aboveground carbon density of forests using deep learning and multisource remote sensing," *Remote Sensing*, vol. 14, no. 13, p. 3022, 2022.

[19] R. Ballesteros, J. F. Ortega, D. Hernandez, and M. A. Moreno, "Onion biomass monitoring using uav-based rgb imaging," *Precision agriculture*, vol. 19, pp. 840–857, 2018.

[20] É. L. Davin, "Land–climate interactions," 2022.

[21] R. A. Houghton and A. A. Nassikas, "Global and regional fluxes of carbon from land use and land cover change 1850–2015," *Global Biogeochemical Cycles*, vol. 31, no. 3, pp. 456–472, 2017.

[22] Y. Pan, R. A. Birdsey, J. Fang, *et al.*, "A large and persistent carbon sink in the world's forests," *science*, vol. 333, no. 6045, pp. 988–993, 2011.

[23] A. J. Chamberlin, Z. Y.-C. Liu, C. G. Cross, *et al.*, "Improving remote monitoring of carbon stock in tropical forests using machine learning: A case study in indonesian borneo," *Remote Sens*, 2024.

[24] Z. Wang, Y. Zhang, F. Li, *et al.*, "Regional mangrove vegetation carbon stocks predicted integrating uav-lidar and satellite data," *Journal of Environmental Management*, vol. 368, p. 122 101, 2024.

[25] E. Borgogno Mondino, V. Fissore, M. J. Falkowski, and B. Palik, "How far can we trust forestry estimates from low-density lidar acquisitions? the cutfoot sioux experimental forest (mn, usa) case study," *International Journal of Remote Sensing*, vol. 41, no. 12, pp. 4551–4569, 2020.

[26] D. Yin and L. Wang, "Individual mangrove tree measurement using uav-based lidar data: Possibilities and challenges," *Remote Sensing of Environment*, vol. 223, pp. 34–49, 2019.

[27] H. Qin, W. Zhou, Y. Yao, and W. Wang, "Individual tree segmentation and tree species classification in subtropical broadleaf forests using uav-based lidar, hyperspectral, and ultrahigh-resolution rgb data," *Remote Sensing of Environment*, vol. 280, p. 113 143, 2022.

[28] G. G. d. Castro, G. S. Berger, A. Cantieri, *et al.*, "Adaptive path planning for fusing rapidly exploring random trees and deep reinforcement learning in an agriculture dynamic environment uavs," *Agriculture*, vol. 13, no. 2, p. 354, 2023.

[29] X. Li, Y. He, H. Wang, *et al.*, "Thermal inspection of subsurface defects in wind turbine blade segments under the natural solar condition," *IEEE Transactions on Industrial Electronics*, 2023.

[30] J. Wu, Y. Ye, and J. Du, "Multi-objective reinforcement learning for autonomous drone navigation in urban areas with wind zones," *Automation in Construction*, vol. 158, p. 105 253, 2024.

[31] S. A. H. Mohsan, N. Q. H. Othman, Y. Li, M. H. Alsharif, and M. A. Khan, "Unmanned aerial vehicles (uavs): Practical aspects, applications, open challenges, security issues, and future trends," *Intelligent Service Robotics*, vol. 16, no. 1, pp. 109–137, 2023.

[32] T. Raj, F. Hanim Hashim, A. Baseri Huddin, M. F. Ibrahim, and A. Hussain, "A survey on lidar scanning mechanisms," *Electronics*, vol. 9, no. 5, p. 741, 2020.

[33] S. Royo and M. Ballesta-Garcia, "An overview of lidar imaging systems for autonomous vehicles," *Applied sciences*, vol. 9, no. 19, p. 4093, 2019.

[34] X. Huang, G. Mei, J. Zhang, and R. Abbas, "A comprehensive survey on point cloud registration," *arXiv preprint arXiv:2103.02690*, 2021.

[35] N. Lu, J. Zhou, Z. Han, *et al.*, "Improved estimation of aboveground biomass in wheat from rgb imagery and point cloud data acquired with a low-cost unmanned aerial vehicle system," *Plant Methods*, vol. 15, pp. 1–16, 2019.

[36] P. L. Guth, A. Van Niekerk, C. H. Grohmann, *et al.*, "Digital elevation models: Terminology and definitions," *Remote Sensing*, vol. 13, no. 18, p. 3581, 2021.

[37] M. Mielcarek, K. Stereńczak, and A. Khosravipour, "Testing and evaluating different lidar-derived canopy height model generation methods for tree height estimation," *International journal of applied earth observation and geoinformation*, vol. 71, pp. 132–143, 2018.

[38] J. Lisein, M. Pierrot-Deseilligny, S. Bonnet, and P. Lejeune, "A photogrammetric workflow for the creation of a forest canopy height model from small unmanned aerial system imagery," *Forests*, vol. 4, no. 4, pp. 922–944, 2013.

[39] C. J. Okolie and J. L. Smit, "A systematic review and meta-analysis of digital elevation model (dem) fusion: Pre-processing, methods and applications," *ISPRS Journal of Photogrammetry and Remote Sensing*, vol. 188, pp. 1–29, 2022.

[40] S. Huang, D. Price, and S. J. Titus, "Development of ecoregion-based height–diameter models for white spruce in boreal forests," *Forest ecology and management*, vol. 129, no. 1-3, pp. 125–141, 2000.

[41] E. A. Costa, A. F. Hess, D. R. Klein, C. A. G. Finger, *et al.*, "Height-diameter models for araucaria angustifolia (bertol.) kuntze in natural forests," *Journal of Agricultural Science*, vol. 10, no. 8, pp. 132–145, 2018.

[42] F. M. B. Romero, L. A. G. Jacovine, S. C. Ribeiro, *et al.*, "Allometric equations for volume, biomass, and carbon in commercial stems harvested in a managed forest in the southwestern amazon: A case study," *Forests*, vol. 11, no. 8, p. 874, 2020.

[43] V. Singh, A. Tewari, S. P. Kushwaha, and V. K. Dadhwal, "Formulating allometric equations for estimating biomass and carbon stock in small diameter trees," *Forest Ecology and Management*, vol. 261, no. 11, pp. 1945–1949, 2011.

[44] A. Mulatu, M. Negash, and Z. Asrat, "Species-specific allometric models for reducing uncertainty in estimating above ground biomass at moist evergreen afromontane forest of ethiopia," *Scientific Reports*, vol. 14, no. 1, p. 1147, 2024.

[45] W. Draudt, "Zur methode der forsteinrichtung [on the method of forest management planning]," German, *Allgemeine Forst- und Jagdzeitung*, vol. 93, pp. 241–254, 1917.

[46] I. Goodfellow, Y. Bengio, A. Courville, and Y. Bengio, *Deep learning*. MIT press Cambridge, 2016, vol. 1.

[47] Y. LeCun, Y. Bengio, and G. Hinton, "Deep learning," *nature*, vol. 521, no. 7553, pp. 436–444, 2015.

[48] M. D. Zeiler and R. Fergus, "Visualizing and understanding convolutional networks," in *Computer Vision–ECCV 2014: 13th European Conference, Zurich, Switzerland, September 6-12, 2014, Proceedings, Part I 13*, Springer, 2014, pp. 818–833.

[49] J. Gu, Z. Wang, J. Kuen, *et al.*, "Recent advances in convolutional neural networks," *Pattern recognition*, vol. 77, pp. 354–377, 2018.

[50] Z. Li, F. Liu, W. Yang, S. Peng, and J. Zhou, "A survey of convolutional neural networks: Analysis, applications, and prospects," *IEEE transactions on neural networks and learning systems*, vol. 33, no. 12, pp. 6999–7019, 2021.

[51] K. Simonyan and A. Zisserman, "Very deep convolutional networks for large-scale image recognition," *arXiv preprint arXiv:1409.1556*, 2014.

[52] K. He, X. Zhang, S. Ren, and J. Sun, "Deep residual learning for image recognition," in *Proceedings of the IEEE conference on computer vision and pattern recognition*, 2016, pp. 770–778.

[53] A. G. Howard, M. Zhu, B. Chen, *et al.*, "Mobilenets: Efficient convolutional neural networks for mobile vision applications," *arXiv preprint arXiv:1704.04861*, 2017.

[54] M. Tan and Q. Le, "Efficientnet: Rethinking model scaling for convolutional neural networks," in *International conference on machine learning*, PMLR, 2019, pp. 6105–6114.

[55] I. K. Nti, O. Nyarko-Boateng, J. Aning, *et al.*, "Performance of machine learning algorithms with different k values in k-fold cross-validation," *International Journal of Information Technology and Computer Science*, vol. 13, no. 6, pp. 61–71, 2021.

[56] D. Enterprises, *Matrice 300 rtk user manual*, version v3.4, Technical specifications and product overview, May 2023. [Online]. Available: `https://www.dji.com/matrice-300/downloads`.

[57] T. Kersten, J. Wolf, and M. Lindstaedt, "Investigations into the accuracy of the uav system dji matrice 300 rtk with the sensors zenmuse p1 and l1 in the hamburg test field," in *XXIV ISPRS Congress "Imaging today, foreseeing tomorrow", 6–11 June 2022, Nice, France*, Copernicus, 2022, pp. 339–346.

[58] Y. Dong, "The design of autonomous uav prototypes for inspecting tunnel construction environment," *arXiv preprint arXiv:2408.07286*, 2024.

[59] DJI, *Zenmuse l1 user manual*, version v1.2, Available at: `https://www.dji.com/zenmuse-l1`, DJI, Sep. 2021.

[60] M. Štroner, R. Urban, T. Křemen, and J. Braun, "Uav dtm acquisition in a forested area–comparison of low-cost photogrammetry (dji zenmuse p1) and lidar solutions (dji zenmuse l1)," *European Journal of Remote Sensing*, vol. 56, no. 1, p. 2 179 942, 2023.

[61] LandMark Technologies, *Lt800 user manual*, Technical specifications and product overview, LandMark Technologies, USA, 2022.

[62] Shanghai Huace Navigation Technology Ltd. (CHC Navigation), *Lt800 especifications*, Technical specifications and product overview, Nov. 2023. [Online]. Available: `https://www.chcnav.com/product-detail/lt800`.

[63] Haglöf Sweden AB, *Mantax blue product sheet*, Technical specifications and product overview, Sweden, 2014. [Online]. Available: `https://haglofsweden.com/project/mantax-blue`.

[64] Haglöf Sweden AB, *Vertex 5 – heights, distance, and angle*, Technical specifications and product overview, Sweden, 2020. [Online]. Available: `https://haglofsweden.com/project/vertex-5`.

[65] Haglöf Sweden AB, *Vertex 5 – quick guide*, Quick reference guide for the Vertex 5 forest measurement instrument, Sweden, 2020. [Online]. Available: `https://haglofsweden.com/project/vertex-5`.

[66] Haglöf Sweden AB, *Mattson increment borers*, Technical specifications and product overview, Sweden, 2022. [Online]. Available: `https://haglofsweden.com/project/increment-borers`.

[67] D. Enterprise, *DJI Terra*, `https://enterprise.dji.com/dji-terra`, Accessed: April 24, 2025.

[68] Q. G. I. System, *QGIS*, `https://qgis.org`, Accessed: May 19, 2025.

[69] T. Sutton, O. Dassau, and M. Sutton, *Gentle gis introduction*, version 3.40, Brought to you with QGIS, a Free and Open Source Software GIS Application, QGIS Project, Feb. 2025. [Online]. Available: `https://qgis.org/resources/hub`.

[70] rapidlasso GmbH, *Rapidlasso*, `https://rapidlasso.de`, Accessed: May 19, 2025.

[71] K. He, X. Zhang, S. Ren, and J. Sun, "Identity mappings in deep residual networks," in *Computer Vision–ECCV 2016: 14th European Conference, Amsterdam, The Netherlands, October 11–14, 2016, Proceedings, Part IV 14*, Springer, 2016, pp. 630–645.

[72] M. Sandler, A. Howard, M. Zhu, A. Zhmoginov, and L.-C. Chen, "Mobilenetv2: Inverted residuals and linear bottlenecks," in *Proceedings of the IEEE conference on computer vision and pattern recognition*, 2018, pp. 4510–4520.

[73] M. M. Kabir, A. Q. Ohi, M. S. Rahman, and M. F. Mridha, "An evolution of cnn object classifiers on low-resolution images," in *2020 IEEE 17th International Conference on Smart Communities: Improving Quality of Life Using ICT, IoT and AI (HONET)*, IEEE, 2020, pp. 209–213.

[74] Z. Holcomb, *Fundamentals of descriptive statistics*. Routledge, 2016.

[75] A. V. Tatachar, "Comparative assessment of regression models based on model evaluation metrics," *International Research Journal of Engineering and Technology (IRJET)*, vol. 8, no. 09, pp. 2395–0056, 2021.

[76] M. C. Peel, B. L. Finlayson, and T. A. McMahon, "Updated world map of the köppen-geiger climate classification," *Hydrology and earth system sciences*, vol. 11, no. 5, pp. 1633–1644, 2007.

[77] I. P. M. Atmosfera, *Área educativa - CLIMA DE PORTUGAL CONTINENTAL*, `https://www.ipma.pt/pt/educativa/tempo.clima`, Accessed: April 4, 2025.

[78] V. AA, "A vegetação de portugal," *Imprensa Nacional*, 2021.

[79] M. Tomé, S. Barreiro, A. Cortiçada, *et al.*, "Inventário florestal 2005-2006. áreas, volumes e biomassas dos povoamentos florestais. resultados nacionais e por nut's ii e iii," *Publicações GIMREF. RT*, vol. 5, p. 2007, 2007.

[80] I. da Conservação da Natureza e das Florestas, "Ifn6 - sexto inventário florestal nacional: Relatório completo," Instituto da Conservação da Natureza e das Florestas, Tech. Rep., 2015, Relatório Nacional Português. [Online]. Available: `https://www.icnf.pt`.

[81] T. F. Fonseca, A. C. Gonçalves, and J. Lousada, *Maritime pine, its biological and silvicultural traits for the basis of natural resources: An overview*. IntechOpen, 2022.

[82] L. Bouffier, A. Raffin, and R. Alía, "Maritime pine–pinus pinaster ait," *Best practice for tree breeding in Europe*, pp. 65–76, 2013.

[83] R. D. Britto, J. Mendes, V. Grilo, *et al.*, "A deep learning approach for average height estimation in oak colony using rgb images," *OL2A*, 2025.

[84] M. A. Rodrigues, D. M. Lopes, and S. M. Leite, "Tendências passadas do clima em trás-os-montes na predição de impactos futuros na fixação de carbono de povoamentos mistos de quercus pyrenaica e pinus pinaster.," *Silva Lusitana*, vol. 18, 2010.

[85] A. Garcia-Iruela, L. Esteban, P. de Palacios, *et al.*, "Resinous wood of pinus pinaster ait.: Physico-mechanical properties," *BioResources*, vol. 11, no. 2, pp. 5230–5241, 2016.

[86] P. M. Fernandes and E. Rigolot, "The fire ecology and management of maritime pine (pinus pinaster ait.)," *Forest Ecology and Management*, vol. 241, no. 1-3, pp. 1–13, 2007.

[87] J. Lousada, M. Noronha, D. Lopes, and M. Silva, "Relações entre peso, volume e densidade para a madeira de pinheiro bravo (pinus pinaster ait.) cultivado em portugal," *Silva Lusitana*, vol. 16, no. 2, pp. 183–196, 2008.

[88] H. Filipe dos Santos Viana, A. Martins Rodrigues, R. Godina, J. Carlos de Oliveira Matias, and L. Jorge Ribeiro Nunes, "Evaluation of the physical, chemical and thermal properties of portuguese maritime pine biomass," *Sustainability*, vol. 10, no. 8, p. 2877, 2018.

[89] M. S. Patrício, C. R. Dias, and L. Nunes, "Mixed-effects generalized height-diameter model: A tool for forestry management of young sweet chestnut stands," *Forest Ecology and Management*, vol. 514, p. 120 209, 2022.

[90] M. Tomé, S. Barreiro, J. A. Paulo, and S. P. Faias, "Selecção de equações para estimação de variáveis da árvore em inventários florestais a realizar em portugal," *Publicações FORCHANGE PT*, vol. 9, 2007.

[91] M. Ricker, G. Gutiérrez-García, D. Juárez-Guerrero, and M. E. Evans, "Statistical age determination of tree rings," *PloS one*, vol. 15, no. 9, e0239052, 2020.

[92] X. Arnan, B. López, J. Martínez-Vilalta, M. Estorach, and R. Poyatos, "The age of monumental olive trees (olea europaea) in northeastern spain," *Dendrochronologia*, vol. 30, no. 1, pp. 11–14, 2012.

[93] M. Tomé, S. Faias, and A. Correia, "Equações de biomassa e de volume desenvolvidas no âmbito do tratamento dos dados do inventário florestal nacional 2005–2006," *PublicaçõesGIMREF. RT*, vol. 4, p. 2007, 2007.

[94] L. S. Heath, M. Hansen, J. E. Smith, and P. D. Miles, "Investigation into calculating tree biomass and carbon in the fiadb using a biomass expansion factor approach," in *In: McWilliams, Will; Moisen, Gretchen; Czaplewski, Ray, comps. Forest Inventory and Analysis (FIA) Symposium 2008; October 21-23, 2008; Park City, UT. Proc. RMRS-P-56CD. Fort Collins, CO: US Department of Agriculture, Forest Service, Rocky Mountain Research Station. 26 p.*, vol. 56, 2009.

[95] J. Houghton, L. Meira Filho, B. Lim, *et al.*, *Revised 1996 intergovernmental panel on climate change guidelines for national greenhouse inventories. paris: Ipcc*, 1997.

[96] R. Kongsager, J. Napier, and O. Mertz, "The carbon sequestration potential of tree crop plantations," *Mitigation and Adaptation Strategies for Global Change*, vol. 18, pp. 1197–1213, 2013.

[97] C. Hopkinson, L. Chasmer, C. Young-Pow, and P. Treitz, "Assessing forest metrics with a ground-based scanning lidar," *Canadian Journal of Forest Research*, vol. 34, no. 3, pp. 573–583, 2004.

[98] J. Estornell, L. Ruiz, B. Velázquez-Martí, and A. Fernández-Sarría, "Estimation of shrub biomass by airborne lidar data in small forest stands," *Forest Ecology and Management*, vol. 262, no. 9, pp. 1697–1703, 2011.

[99] M. Hubacek, V. Kovarik, and V. Kratochvíl, "Analysis of influence of terrain relief roughness on dem accuracy generated from lidar in the czech republic territory," *The international archives of the photogrammetry, remote sensing and spatial information Sciences*, vol. 41, pp. 25–30, 2016.

[100] D. G. Território, *Ortofotos 25 cm - zona norte de Portugal Continental - 2021*, `https://www.dgterritorio.gov.pt/dados-abertos`, Accessed: May 20, 2025.

[101] G. E. Engine, *Sentinel-2 Datasets in Earth Engine*, `https://developers.google.com/earth-engine/datasets/catalog/sentinel`, Accessed: May 20, 2025.

[102] C. Sun, A. Shrivastava, S. Singh, and A. Gupta, "Revisiting unreasonable effectiveness of data in deep learning era," in *Proceedings of the IEEE international conference on computer vision*, 2017, pp. 843–852.

[103] R. Chevalier, A. Catapano, R. Pommier, and M. Montemurro, "A review on properties and variability of pinus pinaster ait. ssp. atlantica existing in the landes of gascogne," *Journal of Wood Science*, vol. 70, no. 1, p. 14, 2024.

[104] J. F. S. Luis and T. F. Fonseca, "The allometric model in the stand density management of pinus pinaster ait. in portugal," *Annals of forest science*, vol. 61, no. 8, pp. 807–814, 2004.

[105] L. F. d. S. T. Nunes, "Modelo para a predição de indicadores de gestão florestal sustentável em povoamentos de pinheiro bravo em portugal," Ph.D. dissertation, Universidade Tecnica de Lisboa (Portugal), 2011.

[106] A. L. M. Monteiro, "Avaliação do sucesso da regeneração natural em povoamentos de pinheiro bravo na companhia das lezírias," M.S. thesis, Universidade de Lisboa (Portugal), 2016.

[107] M. Sivakumar, S. Parthasarathy, and T. Padmapriya, "Trade-off between training and testing ratio in machine learning for medical image processing," *PeerJ Computer Science*, vol. 10, e2245, 2024.

[108] I. Muraina, "Ideal dataset splitting ratios in machine learning algorithms: General concerns for data scientists and data analysts," in *7th international Mardin Artuklu scientific research conference*, 2022, pp. 496–504.

[109] A. Peryanto, A. Yudhana, R. Umar, *et al.*, "Klasifikasi citra menggunakan convolutional neural network dan k fold cross validation," *Journal of Applied Informatics and Computing*, vol. 4, no. 1, pp. 45–51, 2020.

[110] A. Sandim, M. E. Silva, P. Fernandes, and T. Fonseca, "Enhancing sustainability and yield in maritime pine forests: Evaluating silvicultural models for natural regeneration," *Land*, vol. 13, no. 2, p. 170, 2024.